JOURNAL OF GEOPHYSICAL RESEARCH, VOL. 114, D09304, doi:10.1029/2008JD011040, 2009

Cirrus observations in the tropical tropopause layer over the western Pacific

M. Fujiwara,[1] S. Iwasaki,[2] A. Shimizu,[3] Y. Inai,[1] M. Shiotani,[4] F. Hasebe,[1] I. Matsui,[3] N. Sugimoto,[3] H. Okamoto,[5] N. Nishi,[6] A. Hamada,[6] T. Sakazaki,[1] and K. Yoneyama[7]

Received 26 August 2008; revised 1 December 2008; accepted 26 January 2009; published 8 May 2009.

[1] A polarization lidar was continuously operated aboard the research vessel Mirai in the tropical western Pacific over three northern winters: at 2.0°N, 138.0°E during November and December 2001; at 2.0°N, 138.5°E during November and December 2002; and at 7.5°N, 134.0°E during December 2004 and January 2005. Intensive radiosonde soundings were made from the vessel at 3-h intervals during all three campaigns. The mechanisms that underlie the observed variations in cirrus in the tropical tropopause layer (TTL) are discussed from the viewpoint of large-scale dynamics and transport. During the 2001 campaign, the tropopause region was cold, but the TTL was often clear, with only some subvisual cirrus. Potential vorticity data and trajectories show that the TTL during this period was strongly affected by dry air transport from the northern midlatitude lower stratosphere. During the 2002 campaign, a packet of large-amplitude equatorial Kelvin waves was the primary control on the generation and disappearance of cirrus in the TTL. During the 2004–2005 campaign, a cold phase of large-scale waves resulted in cirrus generation in the TTL in late December of 2004, similar to that observed during the 2002 campaign. Outflow from the South Pacific Convergence Zone (SPCZ) caused optically thick cirrus in the TTL, particularly during early January 2005, when we also observed regular diurnal variations in cirrus development within the TTL, that is, apparent sedimentation during the nighttime. We investigated two possible controlling processes, namely, horizontal advection together with diurnal variations in convective activity within the SPCZ and diurnal variations in local temperature due to tides and gravity waves. In the equatorial western Pacific, equatorial Kelvin waves are the important dynamical process that controls cirrus variations in the TTL. Dry-air horizontal transport from the midlatitude lower stratosphere and wet-air vertical transport near the tropical convergence regions should also be considered in fully explaining the cirrus observations in the TTL.

Citation: Fujiwara, M., et al. (2009), Cirrus observations in the tropical tropopause layer over the western Pacific, *J. Geophys. Res.*, *114*, D09304, doi:10.1029/2008JD011040.

1. Introduction

[2] Cirrus clouds in the tropical tropopause layer (TTL) represent the key to understanding the dehydration mechanisms of air entering the stratosphere. In the 1980s, it was argued that the absence of a thick, uniform cloud layer near the tropical tropopause contradicts the proposed contribution of slow mean ascent associated with Brewer-Dobson circulation to the dehydration of such air [*Robinson*, 1980; *Holton*, 1984]. Subsequent studies examined the role of cumulonimbus clouds or "hot towers" in the dehydration [e.g., *Johnston and Solomon*, 1979; *Danielsen*, 1982, 1993]. In the 1990s, however, observations made from satellites [e.g., *Wang et al.*, 1996; *Winker and Trepte*, 1998] and aircraft [e.g., *Jensen et al.*, 1996] revealed that optically thin, sometimes subvisual, cirrus clouds are frequently and globally present near the tropical tropopause. Subvisual cirrus is defined as cirrus whose visible optical depth is <0.03 [*Lynch and Sassen*, 2002]; however, as described below, there exist various types of cirrus in the TTL, with various optical depth values. Thus, there is no reason to limit our discussion to subvisual cirrus. *Luo et al.* [2003] summarized the properties of tropical cirrus clouds on the basis of the results of observational and modeling studies. Recent measurements made by satellite-borne lidars have enhanced the climatological information available regarding

---

[1] Graduate School of Environmental Science, Hokkaido University, Sapporo, Japan.

[2] National Defense Academy, Yokosuka, Japan.

[3] National Institute for Environmental Studies, Tsukuba, Japan.

[4] Research Institute for Sustainable Humanosphere, Kyoto University, Uji, Japan.

[5] Graduate School of Science, Tohoku University, Sendai, Japan.

[6] Graduate School of Science, Kyoto University, Kyoto, Japan.

[7] Japan Agency for Marine-Earth Science and Technology, Yokosuka, Japan.

0148-0227/09/2008JD011040$09.00

cirrus in the TTL [*Dessler et al.*, 2006a, 2006b; *Eguchi et al.*, 2007; *Fu et al.*, 2007; *Sassen et al.*, 2008].

[3] Cirrus clouds in the TTL have the potential to strongly influence the heating rate, both locally and remotely, and thus may control vertical motion in the TTL and in the lower stratosphere [e.g., *Doherty et al.*, 1984; *Ackerman et al.*, 1988; *Hartmann et al.*, 2001; *Corti et al.*, 2006]. This cirrus radiative effect is therefore expected to be critical to dehydration efficiency. These cirrus may also influence the radiative budget of the tropical atmosphere. For example, *McFarquhar et al.* [2000] and *Comstock et al.* [2002] estimated the radiative forcings for observed cases, and found that the contributions of cirrus can be significant, depending on their optical depth.

[4] There exist a number of dynamical processes that control the generation, maintenance, and disappearance of cirrus clouds in the TTL. Direct inputs of water vapor and cloud particles by cumulonimbus clouds result in the formation of anvil cirrus [e.g., *Danielsen*, 1982; *Pfister et al.*, 2001; *Massie et al.*, 2002; *Mace et al.*, 2006]. Horizontal transport of air into a large-scale colder region can result in cloud particle formation and dehydration [*Holton and Gettelman*, 2001]. The existence of thin cirrus layers near the tropopause detached from anvil cirrus [e.g., *Jensen et al.*, 1996; *Winker and Trepte*, 1998] demonstrates the important role of local/regional temperature perturbations by gravity waves [*Potter and Holton*, 1995] and by equatorial Kelvin waves [e.g., *Tsuda et al.*, 1994; *Boehm and Verlinde*, 2000; *Immler et al.*, 2008]. In particular, equatorial Kelvin and Rossby waves generated by organized cumulus clouds in the tropics [*Matsuno*, 1966; *Gill*, 1980] determine the large-scale temperature distribution and flow pattern in the TTL [e.g., *Highwood and Hoskins*, 1998; *Fujiwara and Takahashi*, 2001; *Hatsushika and Yamazaki*, 2003], and strongly influence the cirrus distribution [*Eguchi and Shiotani*, 2004]. It should be noted that in calculations of quasi-horizontal transport using global meteorological analysis data, it may be necessary to consider various waves [*Jensen and Pfister*, 2004] and diabatic ascent due to radiative heating [*Immler et al.*, 2007] in order to simulate cirrus observations in the TTL. Finally, tropical cirrus might occasionally be affected by extratropical wave activity via Brewer-Dobson circulation [*Eguchi and Kodera*, 2007].

[5] In this paper, we present the results of shipborne lidar cirrus measurements undertaken in the tropical western Pacific during the northern winter, the area and time when the TTL is coldest. We undertook three campaigns in different years, for approximately 1 month each time, and observed variable behaviors of cirrus in the TTL, whose time scales ranged from several days to several hours. During all three campaigns, we also made radiosonde sounding from the vessel at 3-h intervals and observed similar time scale variations in the dynamical structure of the TTL. To supplement these intensive single-point measurements, we also utilize global meteorological analysis data and satellite cloud data with the aim of interpreting the cirrus observations mainly from the viewpoint of large-scale meteorology (i.e., the “weather”) in the TTL. The remainder of this paper is organized as follows. Section 2 describes the observations and methods, section 3 presents the measurement results, section 4 provides a detailed interpretation of the observed characteristics, and finally, section 5 lists the main conclusions.

2. Observations and Data Description

[6] Three 1-month observation campaigns were conducted aboard the research vessel Mirai of the Japan Agency for Marine-Earth Science and Technology (JAMSTEC) in the western Pacific during November–December 2001 (cruise number MR01-K05; 2.0°N, 138.0°E), November–December 2002 (MR02-K06; 2.0°N, 138.5°E), and December 2004 to January 2005 (MR04-08; 7.5°N, 134.0°E). The vessel remained stationed around the specified locations for the entirety of each campaign. During each campaign, a two-wavelength (1064 and 532 nm), Mie-scattering lidar with a depolarization measurement capability at 532 nm was installed in a container situated on the observation deck of the vessel. This lidar system is basically the same as that used in a previous *Mirai* campaign (MR01-K02), as described by *Sugimoto et al.* [2002]. Light pulses from a Nd:YAG laser were emitted to the zenith atmosphere, and the backscattering intensity and polarization by aerosols and cloud particles were measured through a 35-cm telescope with photomultiplier tubes for 532 nm and avalanche photodiode for 1064 nm. The lidar was operated continuously during both day and night in all three campaigns. The original range resolution was 6.00 m for the 2001 and 2002 campaigns and 3.75 m for the 2004–2005 campaign; the original temporal resolution was ~10 s for all three campaigns.

[7] The backscattering intensity received at a distance R, $P(R)$, can be written using the so-called lidar equation:

$$P(R) = \frac{C}{R^2}\beta(R)\exp\left[-2\int_0^R \alpha(r)dr\right], \tag{1}$$

where C is the system constant, $\beta(R)$ is the backscattering coefficient of particles and molecules at R, and $\alpha(r)$ is the extinction coefficient of particles and molecules at a distance r. C includes the transmitted laser pulse energy and other system factors. In the actual calculation of the particle component of β at 532 nm, β_{532}, we used a model profile for the molecular component of β (i.e., the Rayleigh scattering) and estimated C (constant for a certain period) using observed P at 4.5–9 km when this altitude region was considered as particle-free. The particle extinction, α_{532}, was neglected in the β_{532} calculation; thus, the derived β_{532} may have been underestimated near the top of optically thick clouds. For example, a cloud layer with an optical depth of 0.05 (0.1) may have resulted in ~10% (~20%) underestimation in β_{532} at the top of the cloud layer. The particle component of β at 1064 nm, β_{1064}, was calibrated indirectly by assuming $\beta_{1064}/\beta_{532} = 1$ for water droplets in low clouds.

[8] Finally, all lidar parameters were averaged over 60 minutes and for 150 m vertically to reduce random noise. As the final noise level was found to be lower for β_{1064} than for β_{532}, particularly for the 2002 and 2004–2005 campaigns, β_{1064} is mainly used for cloud detection in this paper. It was also found that the lidar sensitivity (systematic noise level) increased (decreased) from the 2001 campaign to the 2004–2005 campaign. In other words, the detection limit of thin clouds decreased to the lowest level during the

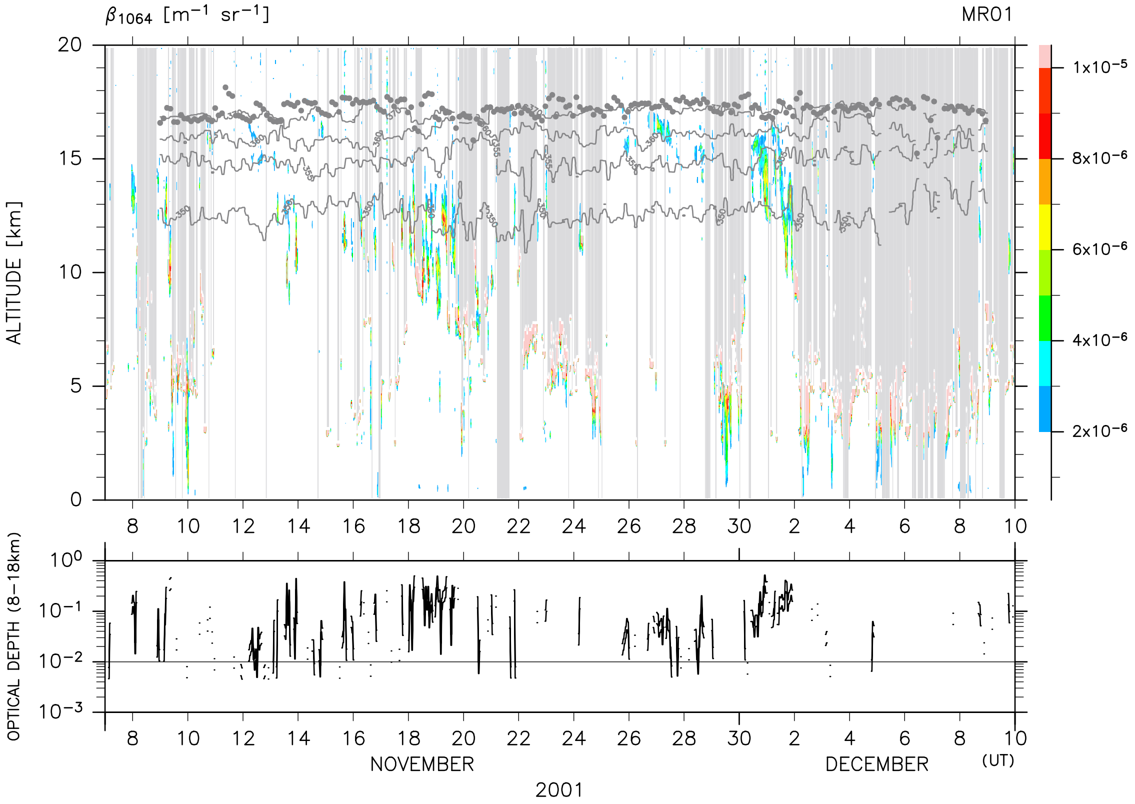

Figure 1. (top) Time-altitude distribution of β_{1064} during the 2001 campaign between 7 November and 10 December 2001. Regions with $\geq 2.0 \times 10^{-6}$ m^{-1} sr^{-1} are colored. Note that universal time (UT) is used and that 0000 UT corresponds to 0900 local time (LT) around the observation site. Regions of missing measurements are shown in light gray (see text for details). The location of the tropopause, as defined by the temperature minimum (i.e., the cold-point tropopause), is indicated by gray dots, and the potential temperature levels of 370, 360, 355, and 350 K are indicated by gray lines. (bottom) Optical depth at 1064 nm estimated by integrating $\beta_{1064} \geq 2.0 \times 10^{-6}$ m^{-1} sr^{-1} from 8 to 18 km and by assuming S to be 15 and 25 sr (see text for details). The calculation is made only when there are no missing measurements in the column.

2004–2005 campaign (note the different coloring used for small β_{1064} values among Figures 1–3), whereas the detection of thicker clouds remained unchanged over the three campaigns. Cumulus clouds were commonly observed around the top of the marine boundary layer during all three campaigns. If such clouds were continuously present for 60 minutes, the entire measurements are considered missing. Furthermore, thick cloud layers in the lower to middle troposphere can prevent the laser light from sensing above the layer. In this paper, if a cloud layer exists with $\beta_{1064} > 1.2 \times 10^{-5}$ m^{-1} sr^{-1}, the measurements above the level that show $\beta_{1064} < 1.0 \times 10^{-5}$ m^{-1} sr^{-1} are also considered missing. Regions of missing measurements are shown in gray in Figures 1–3.

[9] Upper air soundings were conducted during all three campaigns at 3-h intervals. Vaisala RS80H radiosondes were used for the 2001 and 2002 campaigns, and Vaisala RS92 radiosondes for the 2004–2005 campaign. The original vertical resolution was ~5 m. Here, we discuss errors in RS92 temperature and relative humidity (RH) data in detail because in section 4.3.2, we will extensively use these data to investigate diurnal variations in the TTL. The radiosonde temperature measurements are known to suffer from solar heating errors that depend on the solar elevation angle and sensor altitude, among other factors, and that a radiation correction as a function of solar angle and altitude is applied operationally in the ground-data-receiving system. For RS92 temperature sensors, the radiation correction is ≤0.2 K at 121–55 hPa, and the reproducibility in soundings (i.e., overall uncertainty) is estimated to be 0.2 K at 1080–100 hPa and 0.3 K at 100–20 hPa [*Steinbrecht et al.*, 2008; see also *Luers*, 1997].

[10] RS92 RH sensors are known to suffer from time lag errors in low temperatures [e.g., *Miloshevich et al.*, 2004] and solar heating errors that depend on the solar zenith angle, θ, and air pressure, P_a [e.g., *Yoneyama et al.*, 2008], among other factors. In this paper, correction is made for solar heating errors using the same method as that of *Yoneyama et al.* [2008] with eleven Meteolabor Snow White (SW) chilled mirror hygrometer data taken on the same vessel mostly around 0430 universal time (UT) (~1330 local time (LT)) on different days during the 2004–2005 campaign. SW hygrometers have previously been used for validation of Vaisala RH sensors in the tropical troposphere [e.g., *Fujiwara et al.*, 2003a; *Verver et al.*, 2006; *Yoneyama et al.*, 2008], but are known to sometimes show discrepancies with the National Oceanic and Atmospheric Administration (NOAA) frost point

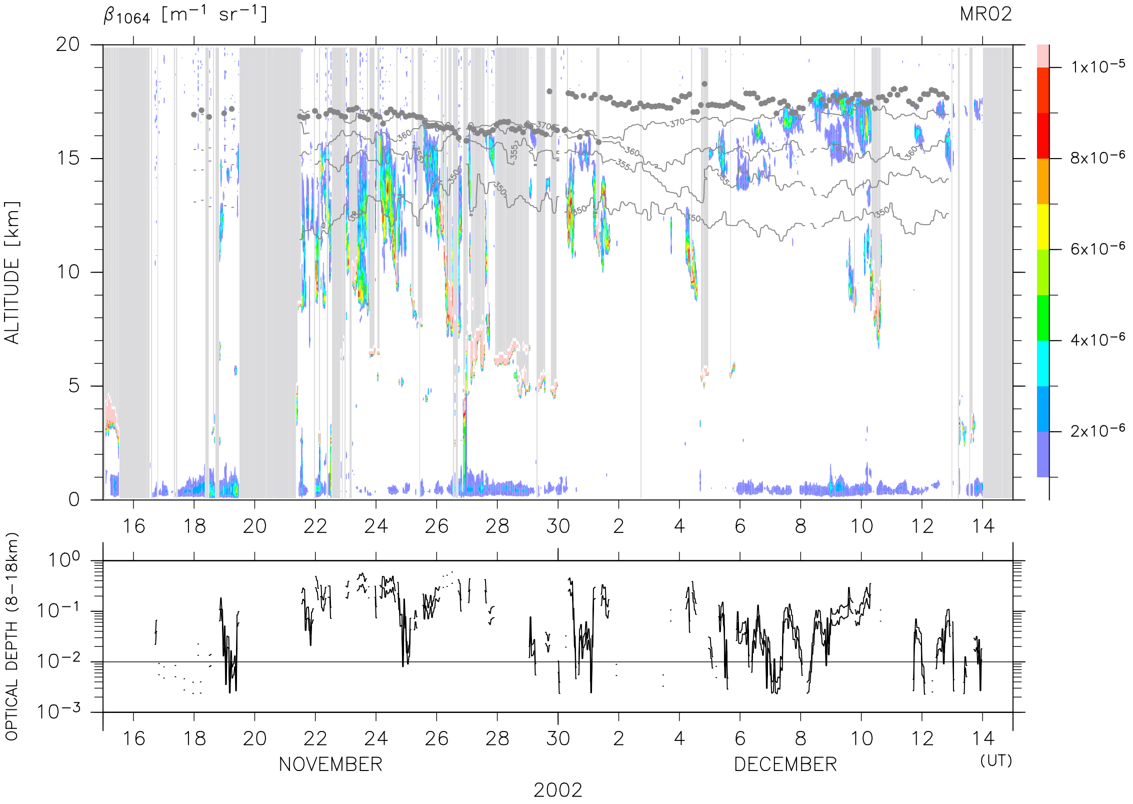

Figure 2. As for Figure 1 but for the 2002 campaign between 15 November and 15 December 2002. Regions with $\geq 1.0 \times 10^{-6}$ m^{-1} sr^{-1} are colored. Optical depths are calculated by integrating $\beta_{1064} \geq 1.0 \times 10^{-6}$ m^{-1} sr^{-1} from 8 to 18 km.

hygrometers around the tropical tropopause [*Vömel et al.*, 2003]. It should be noted that the day-type Snow White hygrometers used here (and used by *Yoneyama et al.* [2008]) were all equipped with a black-colored stainless steel inlet to minimize water vapor contamination. The correction procedure for RS92 RH data is as follows. We choose eleven RS92 data (ten at 0300 UT and one at 0600 UT) as quasi-simultaneous with the eleven SW data. Using this data set, we obtain a mean correction profile, RH$_{dif}$ as

$$\mathrm{RH}_{dif} = c_1(\ln P_a)^2 + c_2(\ln P_a) + c_3, \qquad (2)$$

where $c_1 = -2.53$, $c_2 = 45.88$, and $c_3 = -196.91$. Note that the profile of RH$_{dif}$ is quite similar to that for the equatorial Indian Ocean measurements during October and November 2006 presented by *Yoneyama et al.* [2008]. Then the corrected RH (over water), RH$_{cor}$ is obtained from

$$\mathrm{RH}_{cor} = \left\{100/\left[100 + (\cos\theta/\cos\theta_m) \times \mathrm{RH}_{dif}\right]\right\} \times \mathrm{RH}_{obs}, \qquad (3)$$

where θ_m = 33.0 is the mean solar zenith angle for the eleven RS92 data, and RH$_{obs}$ is RH over water as originally reported from radiosondes. In practice, RS92 data taken at 0000 UT (~0900 LT), 0300 UT (~1200 LT), and 0600 UT (~1500 LT) are only corrected. In section 4.3.2, the corrected RH (over water) data are then translated to RH over ice and water vapor mixing ratio (WVMR) using vapor pressure parameterizations of ice and supercooled water. We use the Goff-1965 parameterizations presented by *Murphy and Koop* [2005] who extensively discussed the uncertainty of various parameterizations. In particular, they pointed out that the parameterizations for supercooled water (needed for the above translations) are extrapolations that were not originally intended for use below the freezing point. In summary, RH over ice and WVMR data in the TTL that will be presented in section 4.3.2 have large uncertainty that cannot be quantitatively estimated at this moment, and should basically be regarded as qualitative.

[11] Global operational analysis data of the European Centre for Medium-Range Weather Forecasts (ECMWF) were used for the analysis of large-scale meteorological fields. The horizontal spacing of the data is 2.5° × 2.5°, the vertical levels are 250, 200, 150, 100, and 70 hPa in and around the TTL, and the time resolution is twice daily. Other global analysis data sets are also used for comparison (see section 4.2). Daily averaged 2.5° × 2.5° gridded outgoing longwave radiation (OLR) by the NOAA [*Liebmann and Smith*, 1996] is used for the analysis of large-scale organized convective activity. Hourly 0.25° × 0.25° gridded blackbody temperature (Tbb) data from the Geostationary Operational Environmental Satellite 9 (GOES 9) is used for the detection of deep convection that directly affect the TTL for the 2004–2005 campaign (section 4.3.1). Note that between May 2003 and June 2005, GOES 9 was in operation over the western Pacific because of the termination of Geostationary Meteorological Satellite 5 (GMS-5). Air trajectories were calculated using a

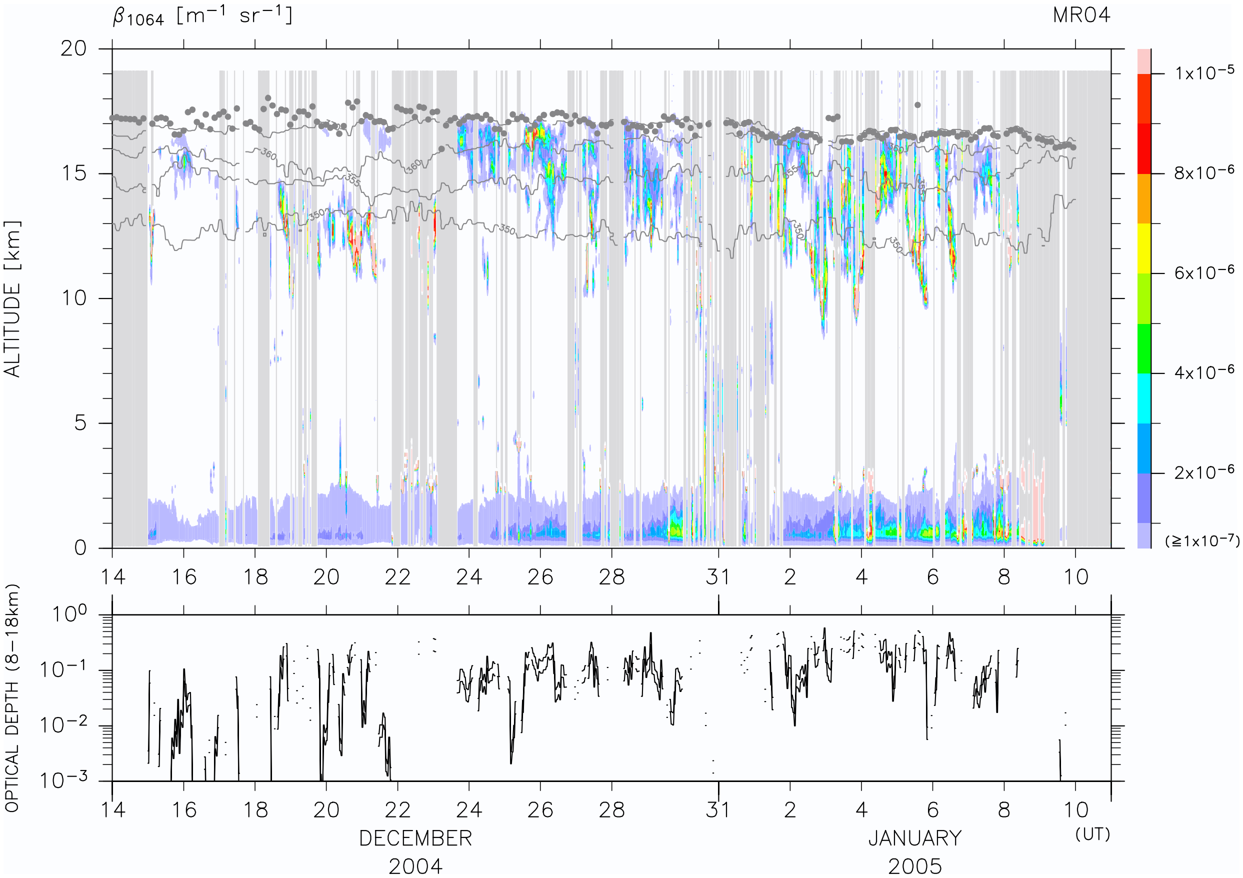

Figure 3. As for Figure 1 but for the 2004–2005 campaign between 14 December 2004 and 11 January 2005. Regions with $\geq 1.0 \times 10^{-7}$ m^{-1} sr^{-1} are colored. Optical depths are calculated by integrating $\beta_{1064} \geq 1.0 \times 10^{-7}$ m^{-1} sr^{-1} from 8 to 18 km.

model developed at the Earth Observation Research Center (EORC), National Space and Development Agency (NASDA) (now Japan Aerospace Exploration Agency, JAXA), as used previously by *Fujiwara et al.* [2003b] and *Hasebe et al.* [2007], among others. This model uses the second-order Runge-Kutta method for time integration and linear interpolation for meteorological data.

3. Results

3.1. Lidar Measurements

[12] Figures 1–3 show the time-altitude distribution of the 1064-nm particle backscattering coefficient β_{1064} (i.e., cloud signal) for the 2001, 2002, and 2004–2005 campaigns, respectively. The difference in lidar sensitivity among the three campaigns is shown by the coloring for $<2.0 \times 10^{-6}$ m^{-1} sr^{-1}. The 2004–2005 lidar system was the most sensitive to optically thin clouds. Gray regions in Figures 1–3 indicate missing measurements due to cumulus clouds around the top of the marine boundary layer and thick cloud layers in the lower to middle troposphere. During the 2001 campaign, thick clouds were frequently observed in the lower to middle troposphere, whereas they were rarely observed during the 2002 and 2004–2005 campaigns. Also shown are the locations of the cold-point tropopause (defined as the coldest point in each temperature profile) and four potential temperature levels measured by radiosondes aboard the vessel. The 350 K potential temperature curve is considered a proxy for the bottom of the TTL, following, for example, *Gettelman and Forster* [2002].

[13] During the 2001 campaign (Figure 1), the TTL was basically clear, with only small numbers of thin, subvisual cirrus clouds. Although, around 20–25 November and early December, thick clouds in the lower to middle troposphere often prevented measurements in the TTL, intermittent penetrations of laser light confirm this observation. *Iwasaki et al.* [2004] described the detailed characteristics of all seven cases of subvisual cirrus observed at 14–17 km during this campaign. The effective radius of these cloud particles was estimated to be 9–16 μm under the assumption of a spherical shape with a number density of 10^5 m^{-3}. All the cirrus showed apparent sedimentation, with an average rate of 2.6 km d^{-1} or 3×10^{-2} m s^{-1} during the nighttime; they tended to disappear around midday. The potential temperature curves for the TTL and the cold-point tropopause shown in Figure 1 do not show significant fluctuations with a time scale of several days; we found no clear evidence of large-amplitude wave activity. The reason for the quasi-cloud-free TTL observed during this campaign is explored in section 4.1.

[14] During the 2002 campaign (Figure 2), the TTL was strongly perturbed with a time scale of 1 week, and the tropopause showed a jump, followed by downward displacement shown in potential temperature curves, during the

middle of the campaign period. These features are typical of the passage of large-amplitude equatorial Kelvin waves in the TTL [e.g., *Fujiwara and Takahashi*, 2001], as will be explained in section 4.2. Cirrus clouds in the TTL showed variations corresponding to the dynamical variation. The clouds were present in late November, disappeared around 1–4 December when downward air mass displacement occurred, and appeared again in the upper part of the TTL after 5 December.

[15] During the 2004–2005 campaign (Figure 3), except for the first quarter of the period, the TTL was largely covered by thick cirrus clouds. Optically thin clouds appeared at 16–17 km around 21 December, immediately after the downward air mass displacement that occurred around 15–20 December. After 23 December, thick clouds persisted in the TTL. The β_{1064} values in the TTL increased during the later days of the campaign. From aboard the vessel, we could even observe these clouds by eye during the daytime when wearing polarizing sunglasses, and by naked eye at sunset. The origin of these "visual" cirrus clouds is discussed in section 4.3.1. Furthermore, in early January we observed a quasi-steady diurnal variation in cirrus within the TTL; namely, apparent sedimentation from the upper TTL to ~10 km through the night. This phenomenon is described in detail and discussed in section 4.3.2.

[16] Also shown in Figures 1–3 is the estimated optical depth at 1064 nm, τ_{1064}, for cloud layers at 8–18 km. The optical depth between the altitudes z_1 and z_2 is written as

$$\tau_{1064} \equiv \int_{z_1}^{z_2} \alpha_{1064} dz = \int_{z_1}^{z_2} S\beta_{1064} dz, \qquad (4)$$

where S is the so-called lidar ratio $\alpha_{1064}/\beta_{1064}$. According to the Mie solution, S ranges from ~15 sr to ~25 sr for 3–200 μm ice particles at both 1064 and 532 nm. For this calculation, we assumed a modified gamma size distribution with dispersion p = 2 for solid ice spheres, and used basically the same look-up tables as those given by *Okamoto et al.* [2007]. In Figures 1–3, we assume a constant S of 15 sr and 25 sr, and show two corresponding optical depth curves, which cover the actual optical depths. The integration was performed for vertical columns with no missing measurements between 8 and 18 km and for cloudy (i.e., colored) regions only. This altitude range for the integration was chosen because during the first half of the 2002 campaign and the second half of the 2004–2005 campaign, the cirrus layers commonly extended from the TTL down to around 10 km altitude. Note that a 500-m-thick cloud layer with a constant $\beta_{1064} = 1 \times 10^{-6}$ m^{-1} sr^{-1} results in an optical depth of 1×10^{-2} if we assume S = 20 sr. For the 2001 and 2002 campaigns, therefore, optical depths of $<1 \times 10^{-2}$ may be within the uncertainty of measurements and assumptions in the data processing. For the 2004–2005 campaign, the lower limit of optical depth may be a tenth of that during the earlier campaigns (i.e., 1×10^{-3}). Note also that the optical depth at 532 nm (i.e., at visible wavelengths) is of the same order of magnitude as that at 1064 nm because the ratio β_{1064}/β_{532} ranges from ~1 to ~1.5 above 9 km (see Figure 4).

[17] For the 2001 campaign, most contributions to the optical depth were derived from the clouds at around 10 km. The optical depth of most cirrus layers in the TTL is within the uncertainty of the optical depth estimation; thus, most cirrus are subvisual. The thicker cirrus in the upper TTL at 26–27 November possessed optical depths of $\sim 5 \times 10^{-2}$, and those in the TTL around 30 November to 1 December possessed optical depths of $\sim 2 \times 10^{-1}$. For the 2002 campaign, the optical depths of cirrus layers were $\leq 3 \times 10^{-1}$ in late November and $\leq 1 \times 10^{-1}$ after 5 December. For the 2004–2005 campaign, the optical depths of cirrus layers in the TTL were $\leq (1\text{–}2) \times 10^{-1}$ in late December and $\leq 3 \times 10^{-1}$ (e.g., on 4 January) in early January.

[18] Figure 4 summarizes the average and standard deviation profiles of β_{1064}, β_{1064}/β_{532}, and the particle depolarization ratio at 532 nm for each campaign. The value of β_{1064}/β_{532} is relevant to the particle size and shape, while the depolarization ratio is relevant to the particle shape; the orientation of particles might also affect these parameters. Cloud droplets with a spherical shape should have zero depolarization. Because the particle-free regions at 4.5–9 km are used as a reference in estimating β_{532}, all panels in Figure 4 below 9 km should be considered as a qualitative view. For the 2001 campaign, the profiles above 13 km correspond to the relatively thick clouds around 26–27 November and 30 November to 1 December. For the 2002 campaign, the profiles above 16 km mainly correspond to the high clouds after 5 December. For all three campaigns, the value of β_{1064}/β_{532} ranges from ~1 to ~1.5, with a slight decrease with altitude, and the particle depolarization ratio increases with altitude. The particle depolarization ratio for the 2004–2005 campaign is about twice as high as that for the other campaigns (see section 4.3.2 and Figure 14 for further details of the 2004–2005 campaign). *Platt et al.* [1987] reported depolarization ratio measurements of tropical cirrus between ~12 and ~15 km at Darwin in northern Australia in March–April 1981. Their result, 0.25–0.3 with a slight increase with height, is similar to the results from the 2001 and 2002 campaigns.

3.2. General Descriptions of Large-Scale Meteorology

[19] Figure 5 shows the longitude-time distributions of ECMWF temperature at 360 K, a representative level for the upper part of the TTL, at 2.5°N for the 2001 and 2002 campaigns and at 7.5°N for the 2004–2005 campaign. Figure 6 shows the longitude-time distributions of OLR averaged for 7.5°S–7.5°N, an indicator of the organized convective activity in the tropics. The location of the vessel over time is also shown in Figures 5 and 6. Prominent features over the Indian Ocean, the Indonesian maritime continent, and the western to central Pacific (around 60°E–150°W) are eastward moving cold regions (<194 K) in the TTL and associated organized convection (<200 W m^{-2}) in the troposphere. The cold anomalies in the TTL generally range from 10°S to 10°N, and are commonly equatorially symmetric (see Figure 7 for the 2001 case). These TTL disturbances often have the characteristics of equatorial Kelvin waves [e.g., *Parker*, 1973; *Fujiwara and Takahashi*, 2001], as will be shown in section 4.2 for the 2002 case. The eastward moving convective disturbances in the troposphere are categorized either as convectively coupled equatorial Kelvin waves for a zonal phase speed, $c^{(x)}$, of ~15–20 m s^{-1} [*Wheeler et al.*, 2000], or as convection associated with the Madden-Julian Oscillation (MJO) for $c^{(x)}$ ~5 m s^{-1} [e.g., *Madden and Julian*, 1994; *Zhang*, 2005]. For the 2002 case,

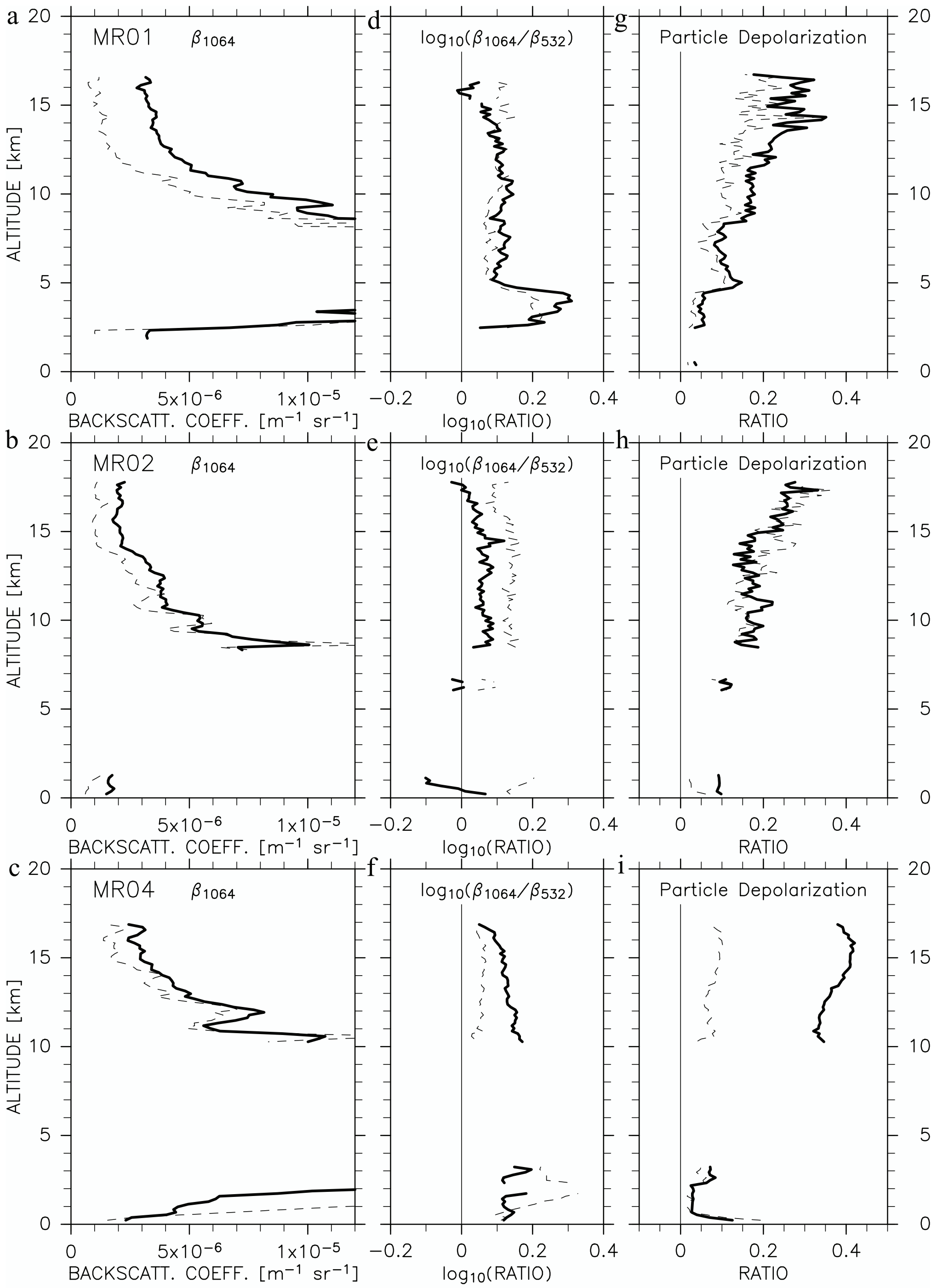

Figure 4. Average (thick solid lines) and standard deviation (thin dashed lines) profiles of (a–c) β_{1064}, (d–f) logarithm of the ratio β_{1064}/β_{532}, and (g–i) the particle depolarization ratio at 532 nm for the 2001 campaign (Figures 4a, 4d, and 4g), the 2002 campaign (Figures 4b, 4e, and 4h), and the 2004–2005 campaign (Figures 4c, 4f, and 4i). The averages are taken only from those regions with β_{1064}, $\beta_{532} \geq 2 \times 10^{-6}$ m^{-1} sr^{-1} for the 2001 campaign and with β_{1064}, $\beta_{532} \geq 1 \times 10^{-6}$ m^{-1} sr^{-1} for the 2002 and 2004–2005 campaigns and only for altitudes with cloud cover of ≥0.02 for the 2001 campaign and ≥0.03 for the 2002 and 2004–2005 campaigns.

$c^{(x)}$ is ~8 m s^{-1}. In other longitudinal regions in Figures 5 and 6, we see several eastward moving waves in the TTL without associated, significant deep convection in the troposphere.

[20] During the 2001 campaign, the TTL was relatively constantly cold over the vessel, and the eastward propagation of the cold anomaly was extremely slow. During the 2002 campaign, a pair of cold and warm anomalies propagated over the vessel. The cloud-free region that occurred during the middle of the campaign period, around 1–4 December (Figure 2), corresponded to the strong warm anomaly of the

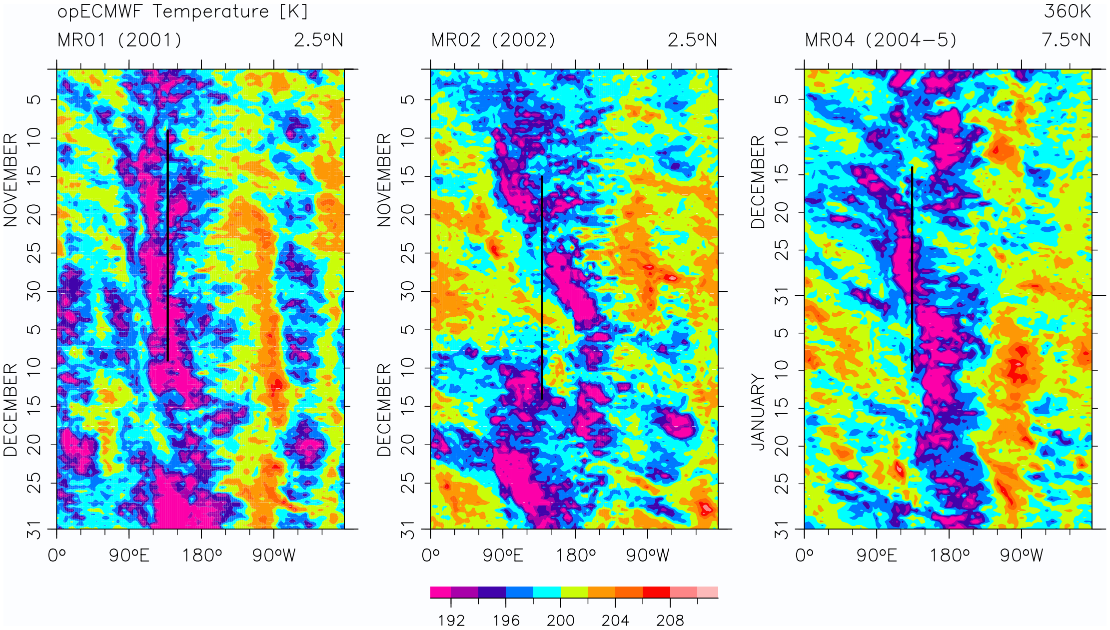

Figure 5. Longitude-time distributions of temperature from operational ECMWF data at 360 K potential temperature (left) for November–December 2001 at 2.5°N, (middle) for November–December 2002 at 2.5°N, and (right) for December 2004 to January 2005 at 7.5°N. The location (longitude) of the vessel over time is shown by the black line in each panel.

wave over the vessel. During the 2004–2005 campaign, the eastward propagation of a cold anomaly was somewhat distorted. The cloud appearance around 21–23 December (Figure 3) corresponded to the arrival of a cold phase of the wave. In early January 2005, the TTL became warm again over the vessel, whereas the cirrus clouds persisted and even thickened in the TTL. It should be noted that for this campaign, most deep convection propagated around the region from 15°S to the equator in the 120°E–150°W longitudinal sector; thus, the vessel (at 7.5°N) was located to the north of the main convective system (see Figure 13).

4. Discussion

4.1. November–December 2001 Campaign

[21] Although temperature conditions were favorable for cirrus generation during the November–December 2001 campaign (Figure 5), only some subvisual cirrus clouds

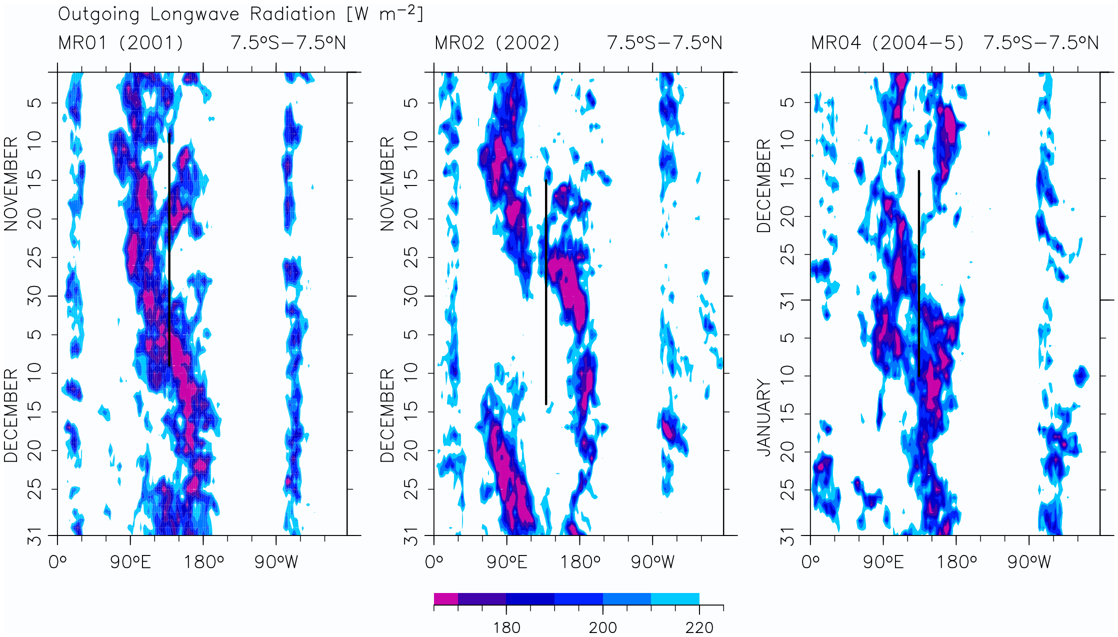

Figure 6. As for Figure 5 but for interpolated outgoing longwave radiation (OLR) averaged for 7.5°S–7.5°N.

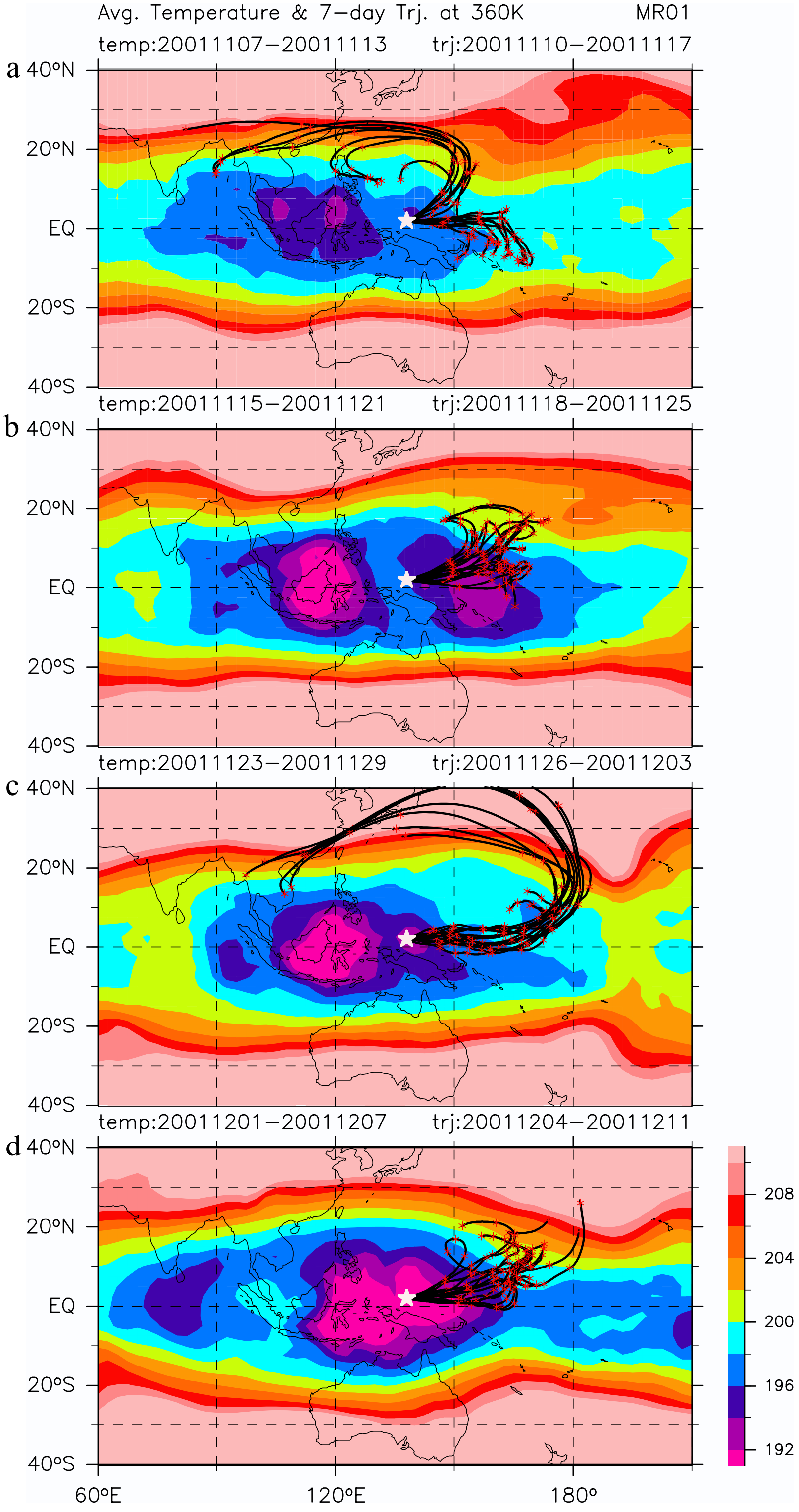

Figure 7. Average temperature distribution at 360 K potential temperature and 7-day backward trajectories (black lines) at the same level starting at 0000 UT over the vessel (shown by white stars) for the 2001 campaign, (a) for 7–13 November for temperature (*T*) and for 10–17 November for the initial dates for trajectories (IDT), (b) for 15–21 November for *T* and for 18–25 November for IDT, (c) for 23–29 November for *T* and for 26 November to 3 December for IDT, and (d) for 1–7 December for *T* and for 4–11 December for IDT. The time period for temperature average for each panel is chosen such that the temperature distribution is representative for the eight 7-day trajectories shown on each panel. Red asterisks on the trajectories represent 1-day intervals.

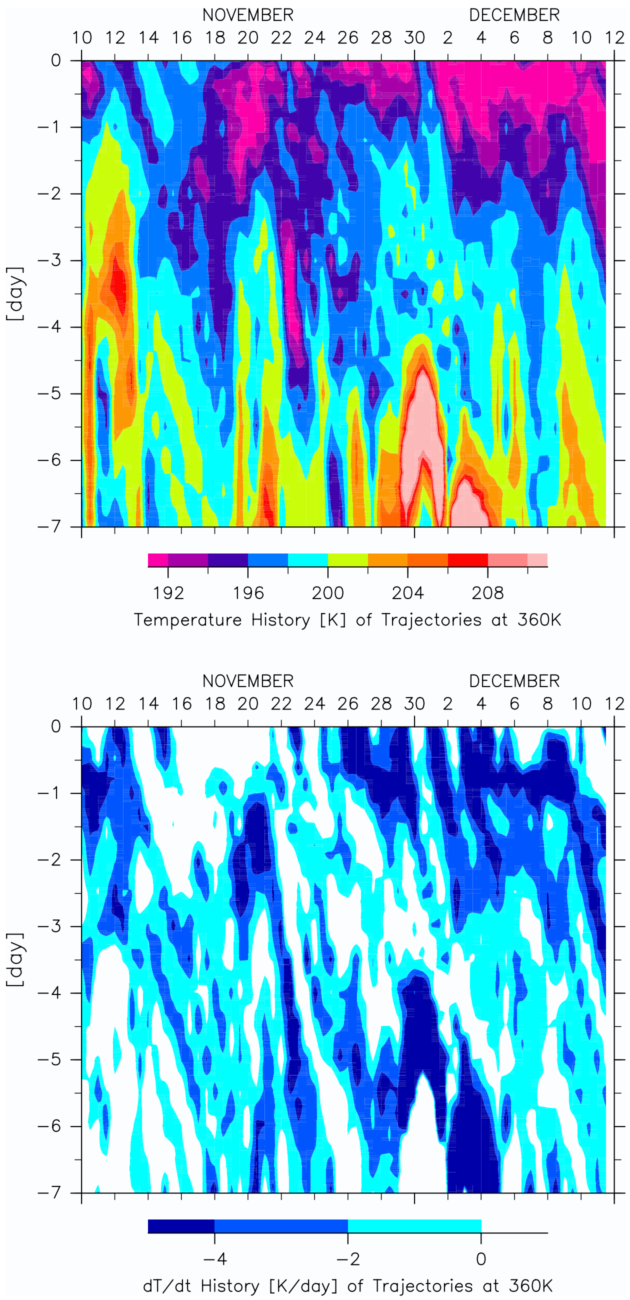

Figure 8. (top) History of temperature and (bottom) time derivative of temperature (*dT*/*dt*) along all the backward trajectories shown in Figure 7. The top horizontal axis shows the initial (starting) date of trajectories, and the vertical axis shows the days from the initial date for each backward trajectory. For Figure 8 (bottom), only negative regions are colored.

were observed in the TTL. In this section, to explain this quasi-cloud-free situation, we investigate the large-scale meteorological conditions by performing trajectory and potential vorticity analyses. Figure 7 shows 7-day backward trajectories at 360 K, starting over the vessel, together with the average temperature distributions at the same level for the four periods of the campaign. Figure 8 shows the temperature history and temperature tendency history along these trajectories. At least in the 1st and 3rd periods, the air was transported from the northern midlatitudes within 1 week, and lidar measurements revealed that the TTL was largely cloud-free. The OLR data show no significant convective activity below these trajectories (not shown); therefore, the air mass identity is considered to have been retained for the 7 days. During the second half of the campaign period, the air temperature was low near the vessel, and the air became colder during transport within a day or two of arrival over the vessel; however, these temperature changes were ineffective in terms of cirrus generation.

[22] *Fujiwara et al.* [2003b] performed ozonesonde measurements at two equatorial stations in western Indonesia over September–October 1998, and observed a case in which an ozone-enhanced layer with a thickness of 1–1.5 km developed just below the tropopause in 1 week at both stations. The authors analyzed the relevant meteorological data, including using the so-called reverse domain filling (RDF) potential vorticity (PV) analysis. RDF analysis, which utilizes backward trajectory calculations, can reproduce fine-scale structures in the PV field [e.g., *Newman and Schoeberl*, 1995]. *Fujiwara et al.* [2003b] concluded that the enhanced ozone originated from the northern midlatitude lower stratosphere around the central Pacific, where active Rossby wave breaking events often cause quasi-horizontal, subtropical stratosphere-troposphere exchange [e.g., *Postel and Hitchman*, 1999; *Waugh and Polvani*, 2000]. It should be noted that the ozone-enhanced layer was observed when the large-scale wave activity was low around the equatorial tropopause, a situation similar to that during the 2001 campaign (e.g., potential temperature curves in Figure 1). Under such a condition, layering structures in tracers would tend to remain undisturbed.

[23] Here, we use the same method as that employed by *Fujiwara et al.* [2003b]: RDF PV analysis. Figure 9 shows the daily distribution of ±2 potential vorticity unit (pvu, equivalent to 10^{-6} K m^2 kg^{-1} s^{-1}), a proxy for the subtropical tropopause, at 360 K for the three campaigns. These ±2 pvu distributions were obtained using the RDF method with 1° × 1° initial points for 3-day backward trajectory calculations (see *Fujiwara et al.* [2003b] for technical details). During the 2001 campaign, the region near the vessel was sometimes even covered by ±2 pvu contours (i.e., the midlatitude lower stratospheric dry air) derived mainly from the northern central Pacific. In contrast, during the 2004–2005 campaign the region near the vessel was relatively isolated from the ±2-pvu midlatitude air. The situation during the 2002 campaign was possibly similar to that during the 2001 campaign; however, large-amplitude waves primarily controlled cirrus variations in the TTL during the 2002 campaign, as will be discussed in section 4.2. Figure 10 shows the frequency distributions of potential vorticity at 360 K around the vessel. The frequency distribution for the 2001 campaign is skew about 0 pvu, the average value at the equator; the frequency is high at 1–2 pvu, indicating influence of northern midlatitude lower stratosphere. (Note that *Postel and Hitchman* [1999] used ±1.5 pvu as a proxy for the subtropical tropopause.) On the other hand, the distribution is almost symmetrical about 0 pvu with very small contributions from >1-pvu and <−1-pvu air for the 2004–2005 campaign. It should be noted that the northward

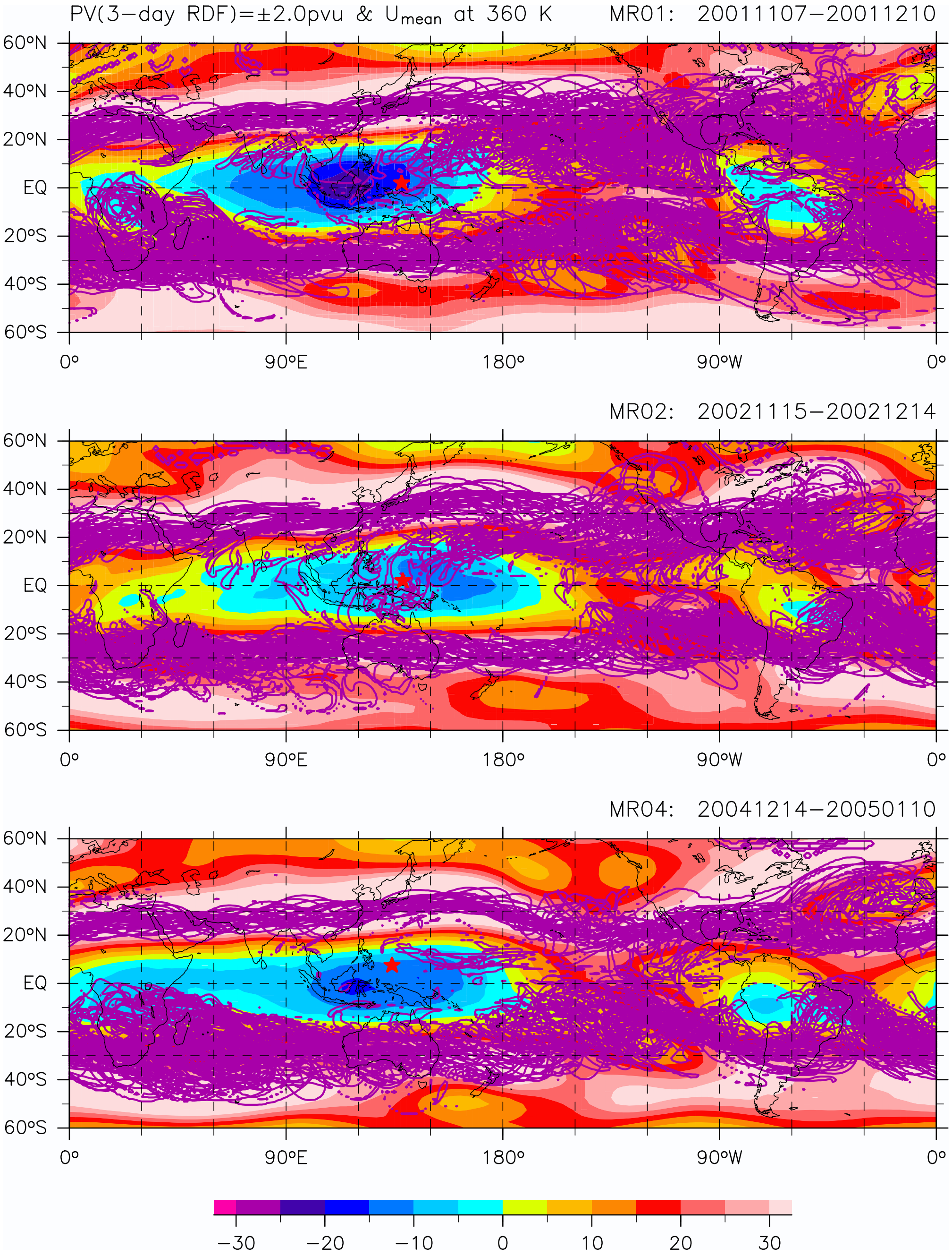

Figure 9. Distributions of daily ±2 potential vorticity unit (pvu, equivalent to 10^{-6} K m^2 kg^{-1} s^{-1}) at 0000 UT (light purple curves) and average zonal wind at 360 K potential temperature (colored) (top) for 7 November to 10 December 2001 (the 2001 campaign), (middle) for 15 November to 14 December 2002 (the 2002 campaign), and (bottom) for 14 December 2004 to 10 January 2005 (the 2004–2005 campaign). The potential vorticity distributions were calculated using the reverse domain filling (RDF) method with 1° × 1° initial points for 3-day backward trajectory calculations. The location of the vessel in each panel is shown by a red star.

gradients of water vapor are negative on average around the northern subtropical tropopause in November–December [*Randel et al.*, 2001, Plate 1]. Therefore, we conclude that the quasi-cloud-free TTL during the 2001 campaign was due to the frequent transport of dry air from the northern midlatitude lower stratosphere, with an additional contribution from low wave activity in the TTL.

[24] *Waugh and Polvani* [2000] found that Rossby wave breaking events that transport midlatitude lower stratospheric air deeply, and thus irreversibly, into the tropical upper troposphere occur predominantly in the eastern Pacific and Atlantic during the northern winter, where and when the so-called equatorial westerly ducts develop as part of the Walker circulation. Mean westerly winds in the tropics enable the midlatitude Rossby waves to penetrate deeply

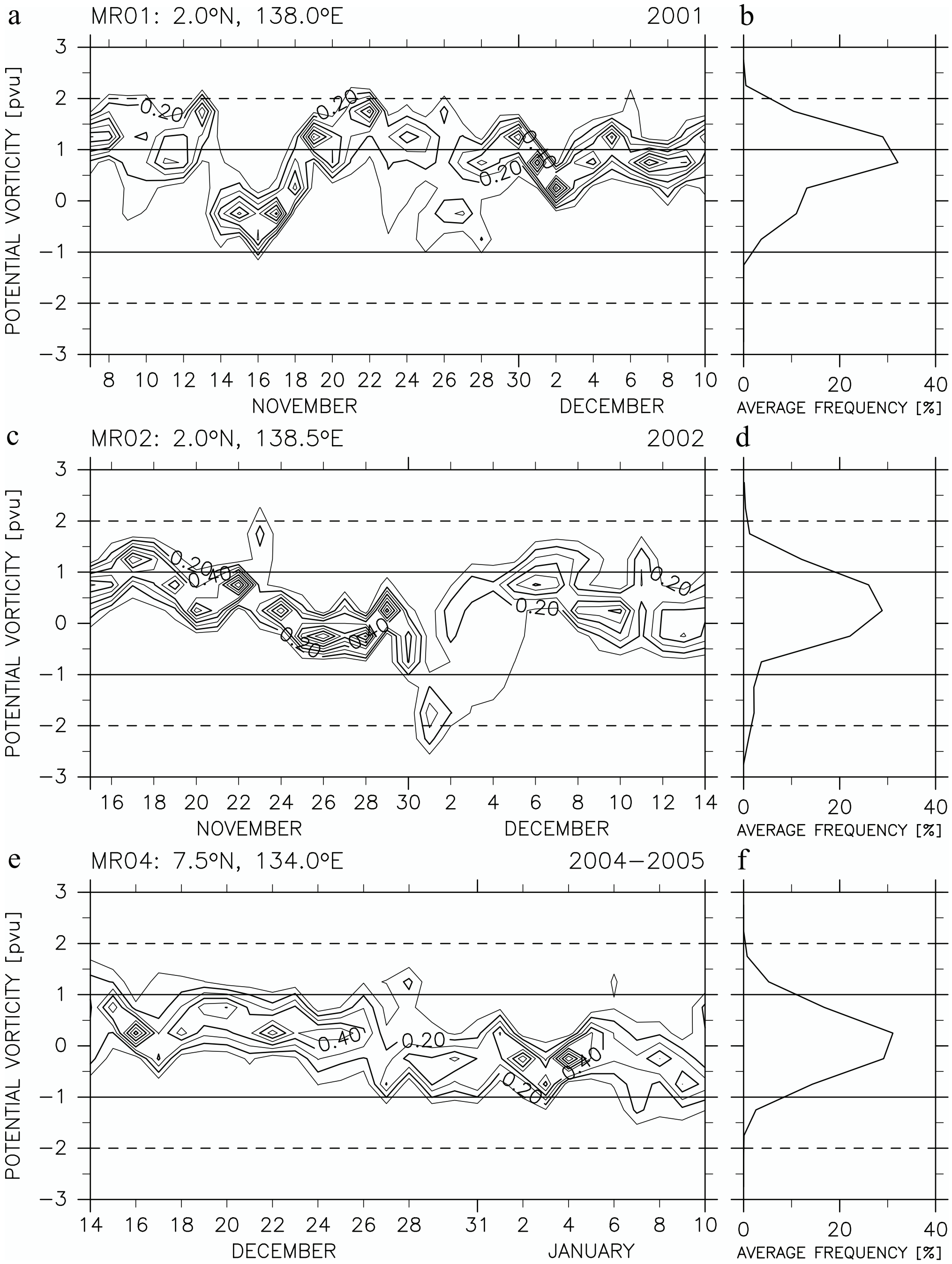

Figure 10. Frequency distributions of potential vorticity at 360 K potential temperature over the region within 5° distance from the vessel (a and b) for the 2001 campaign, (c and d) for the 2002 campaign, and (e and f) for the 2004–2005 campaign using the same 1° × 1° RDF data set as in Figure 9. The temporal variations (Figures 10a, 10c, and 10e) and average for the campaign period (Figures 10b, 10d, and 10f) are shown. The frequency is calculated daily (at 0000 UT) for 81 (for the 2001 campaign) or 78 (for the 2002 and 2004–2005 campaigns) grid points with 0.5-pvu bins.

into the tropics, where they eventually break to result in irreversible horizontal mixing and dry-air intrusion. The authors also noted that the westerly duct in the eastern Pacific is stronger (i.e., wider in longitude and greater in magnitude) during the cold phases of El Niño–Southern Oscillation (ENSO) (La Niña years) and that the number of intrusion events is greater during these years. In fact, Figure 9 shows that deep intrusions of midlatitude air are observed primarily in the tropical eastern Pacific and tropical Atlantic where the mean field is westerly, and that the eastern Pacific westerly duct was stronger for the 2001 campaign (a cold phase) than for the 2002 (a warm phase) and 2004–2005 campaigns (a warm phase) (the climate conditions here are determined from the NINO.3 index prepared by the NOAA). However, the transport into the tropical western Pacific is indirect and requires additional mechanisms. A

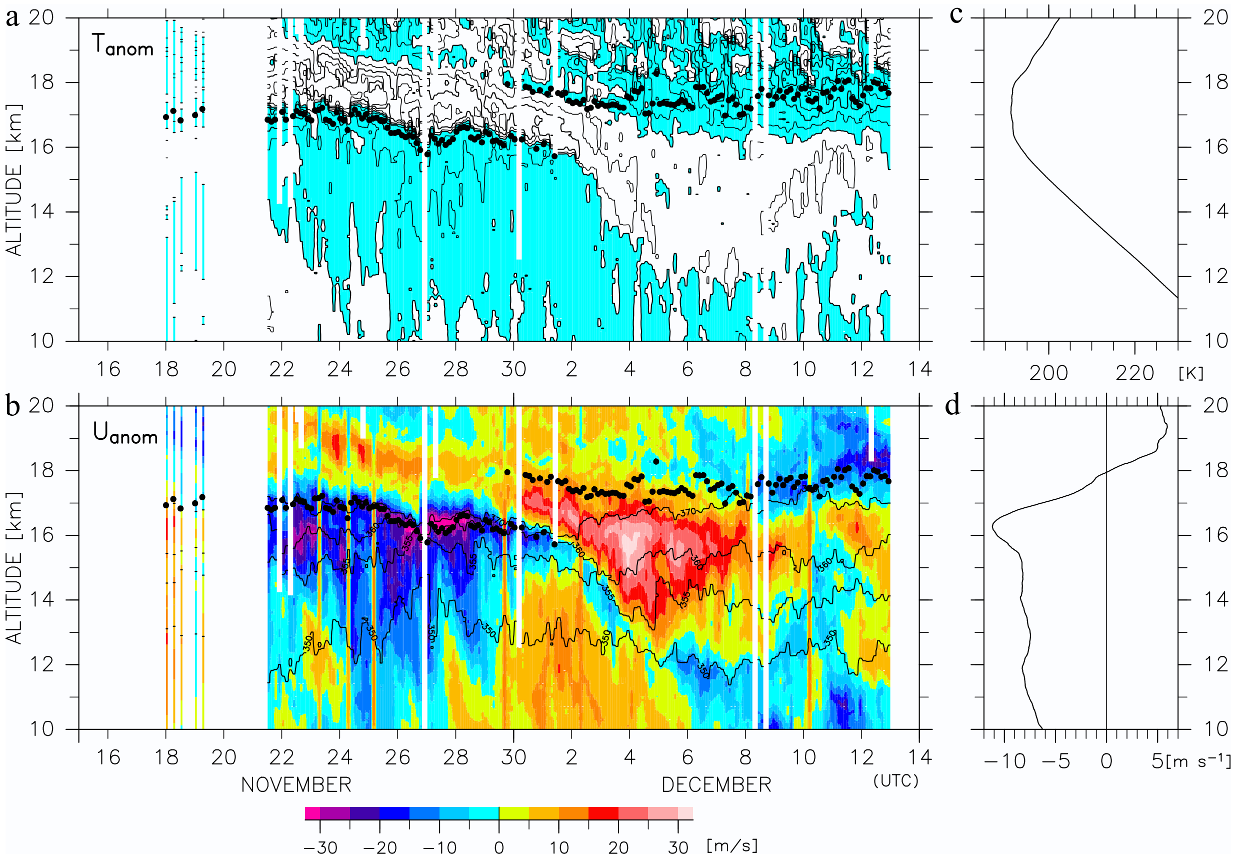

Figure 11. Time-altitude distributions of (a) temperature anomaly and (b) zonal wind anomaly between 15 November and 14 December 2002. In both panels, the location of the cold-point tropopause is indicated by black dots, and the potential temperature levels of 370, 360, 355, and 350 K are indicated by black curves in Figure 11b. In Figure 11a, the contour interval is 2 K, and negative regions are colored blue. The average profiles of (c) temperature and (d) zonal wind.

noticeable feature of the average zonal wind field during the 2001 campaign is the stronger easterlies in the tropical western Pacific, also due to the cold phase of ENSO. These easterlies may have acted to transport the air further to the west after the air from the midlatitude had entered the easterly region. Note that the quasi-isolated TTL observed during the 2004–2005 campaign would be one of the important factors in explaining the persistent, thick cirrus clouds observed during this campaign (see section 4.3.1).

4.2. November–December 2002 Campaign

[25] During the November–December 2002 campaign, the TTL was greatly perturbed with a time scale of 1 week, and the cirrus in the TTL showed corresponding variations (Figure 2). Figure 11 shows the time-altitude distributions of temperature anomaly, zonal wind anomaly, and their average profiles measured by radiosondes launched aboard the vessel. We observe a clear oscillation in both temperature and zonal wind with a period ($2\pi\omega^{-1}$, where ω is the frequency) of 20–24 days in the TTL. The vertical wavelength ($2\pi|m|^{-1}$, where m is the vertical wave number) is estimated as ~8 km in the TTL and ~4 km in the lower stratosphere. (Half the period/wavelength can be estimated, for example, from the length/distance between two zero curves in the temperature anomaly plot.) The background zonal wind, $\overline{u}$, is ~−10 m s^{-1} at 16 km. The background buoyancy frequency, N, as estimated from the average vertical gradient of potential temperature (not shown), is ~1.4×10^{-2} s^{-1} in the TTL and ~2.5×10^{-2} s^{-1} in the lower stratosphere. The zonal phase speed of the wave ($c^{(x)} \equiv \omega/k$, where k is the zonal wave number), as estimated from Figure 5, is ~8 m s^{-1}. These parameters reasonably satisfy the dispersion relation of the equatorial Kelvin waves: $(\omega - k\overline{u}) = -Nk/m$ [e.g., *Andrews et al.*, 1987]. Note that m is negative here because the vertical phase propagation is downward in Figure 11. This downward phase propagation means that the group velocity of the wave is upward. In other words, this wave packet is generated below the TTL, and the wave energy is propagating upward. Furthermore, this disturbance has no substantial meridional wind component (see Figure 12), and the temperature anomalies lead the associated zonal wind anomalies by a fourth cycle; these are also the important characteristics of equatorial Kelvin waves [e.g., *Parker*, 1973].

[26] The amplitude of the wave was quite large; the temperature change due to the wave passage was about 8 K. The zonal wind amplitude, u_{amp}, was ~25 m s^{-1} at 16 km; therefore, the wave breaking condition, $u_{\mathrm{amp}} \simeq (c^{(x)} - \overline{u})$ (i.e., the amplitude is comparable to the intrinsic zonal phase speed), is satisfied, and turbulence enhancement and irreversible mixing are expected around the eastward

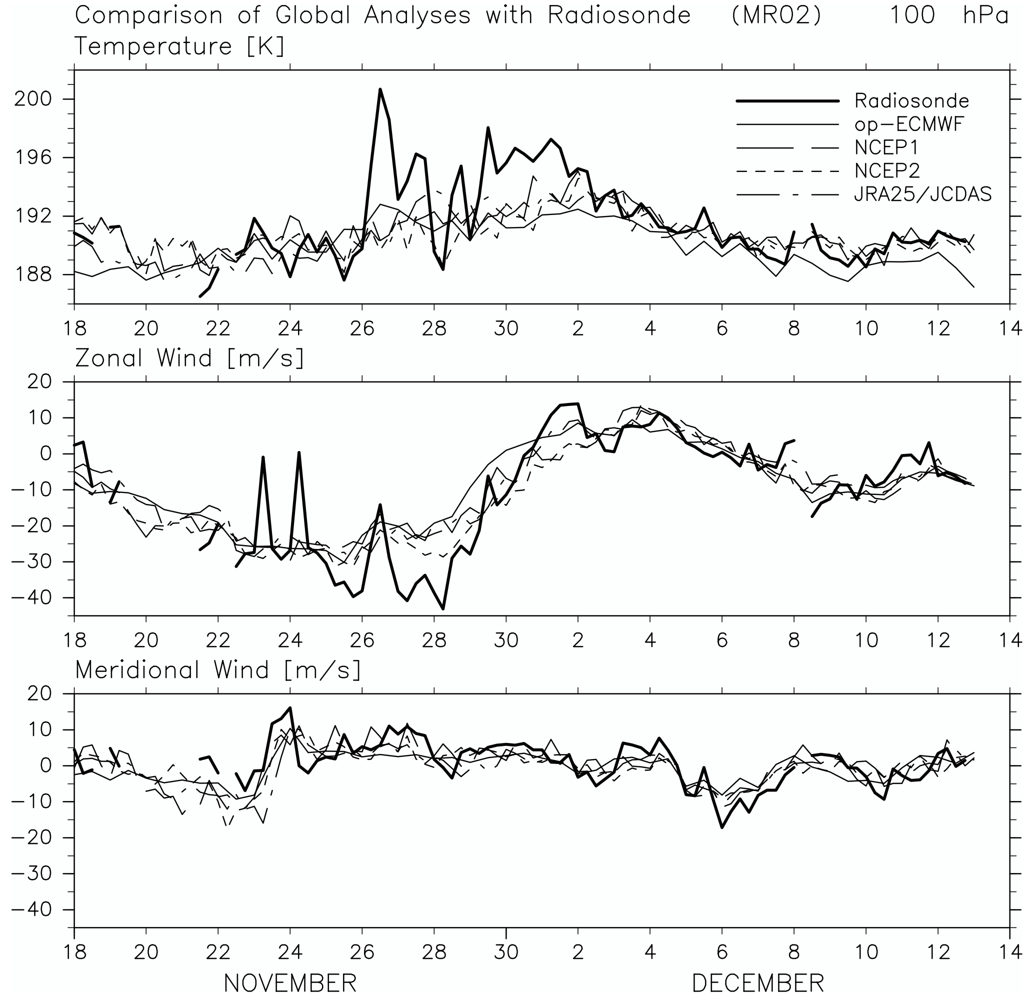

Figure 12. Time series of (top) temperature, (middle) zonal wind, and (bottom) meridional wind at 100 hPa based on radiosonde data (thick solid lines; using only those measurements taken at 0000, 0600, 1200, and 1800 UT), ECMWF operational analysis data (thin solid lines), NCEP1 reanalysis data (dashed lines), NCEP2 reanalysis data (dotted lines), and JRA25/JCDAS reanalysis data (dot-dashed lines). For all four analysis data sets, the horizontal resolution is 2.5°, and the data at four grid points nearest to the observation site are averaged.

wind maximum [*Fujiwara and Takahashi*, 2001; *Fujiwara et al.*, 2003c].

[27] It should be noted that the cold phase corresponds to the upward displacement phase. This means that the sedimentation of cirrus particles should have been in part compensated by the upward wind component of the wave, and the lifetime of cirrus would have been extended. The vertical wind amplitude, w_{amp}, can be estimated from $w_{\mathrm{amp}} = -u_{\mathrm{amp}}\ (k/m)$ to be $\sim 1 \times 10^{-2}$ m s^{-1} in the TTL. (Note that the maximum upward wind leads the maximum upward displacement by a fourth cycle.) Furthermore, as discussed by *Ackerman et al.* [1988] and *Corti et al.* [2006], these cirrus might have acted to reinforce the upward motion via their net radiative heating effect. *Corti et al.* [2006] estimated the mean radiative heating rate in cirrus clouds in the TTL (350–370 K or 13–16 km) to be 1.5 K d^{-1}, which can be roughly translated to $\sim 2 \times 10^{-3}$ m s^{-1}, with substantial variability depending on the vertical extinction profile. Therefore, there may exist an interesting interaction among the vertical motion, cirrus, and radiation at the cold phases of equatorial Kelvin waves in the TTL. On the other hand, at the warm, downward displacement phase, visualized by the deformed potential temperature curves in Figure 2, the dry, ozone-rich air from the lower stratosphere should have prevailed in the TTL [*Fujiwara et al.*, 1998, 2001]. The cirrus clouds disappeared during this period.

[28] Large-amplitude equatorial Kelvin waves are the dominant disturbance in the TTL [e.g., *Nishi et al.*, 2007; *Suzuki and Shiotani*, 2008], and greatly modulate the distributions of ozone, water vapor, and cirrus in the TTL. These waves are primarily generated by large-scale organized convection in the troposphere, such as the MJO [see *Madden and Julian*, 1994, Figure 3] and convectively coupled Kelvin waves [*Wheeler et al.*, 2000]. In the present case, the organized convective system is categorized as the MJO because of its slow zonal phase speed ($\sim$8 m s^{-1}). The disturbance in the TTL, in contrast, can be regarded as equatorial Kelvin waves, based primarily on the fact that the intrinsic phase speed is much higher ($\sim$18 m s^{-1}) because of the background easterly flow in the TTL. In other words,

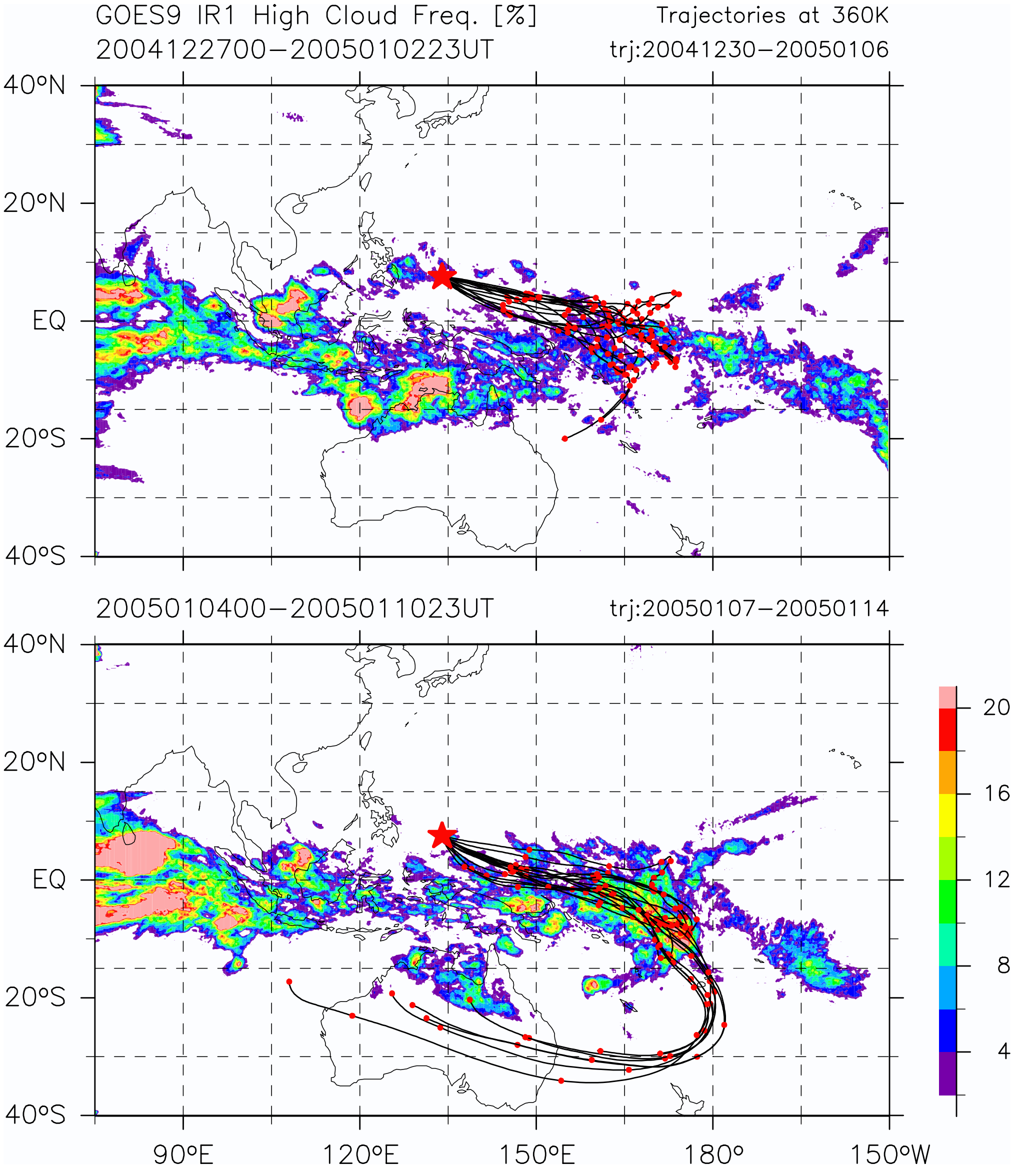

Figure 13. Distributions of high-cloud frequency in percent (i.e., the frequency of blackbody temperatures <210 K at 0.25° × 0.25° grid points) based on GOES 9 IR1 data (top) for 27 December 2004 to 2 January 2005 and (bottom) for 4–10 January 2005. Also shown are the 7-day backward trajectories (black lines) at 360 K potential temperature starting at 0000 UT over the vessel (vessel location is indicated by red stars) for 30 December 2005 to 6 January 2005 (Figure 13, top) and for 7–14 January 2005 (Figure 13, bottom). The time period for trajectories for each panel is chosen such that the trajectories are representative for the high-cloud frequency distribution shown on each panel. Red dots on the trajectories represent 1-day intervals.

the tropical large-scale organized convective system, the MJO, has a direct influence in the TTL over the western Pacific, where the top part of the system can take the form of a "dry" equatorial Kelvin wave "packet," with the observed vertical wavelengths, due to the greater static stability of the background and strong easterly flow. The Kelvin waves in the TTL are not the freely propagating waves found above the middle stratosphere: they are the mode that dissipates at the lowest altitudes (i.e., the TTL) around the top of the latent heat sources.

[29] Finally, we note here that the large-amplitude Kelvin waves in the TTL may sometimes be poorly represented in global analysis data. Figure 12 shows an intercomparison of temperature, zonal wind, and meridional wind at 100 hPa between the radiosondes launched from the vessel and four different global analysis data: the twice-daily ECMWF operational analysis data mainly employed in this paper, four-times-daily NCEP/NCAR reanalysis data (NCEP1) [*Kalnay et al.*, 1996], four-times-daily NCEP-DEO AMIP-II reanalysis data (NCEP2) [*Kanamitsu et al.*, 2002], and four-times-daily Japanese reanalysis data (JRA25/JCDAS) [*Onogi et al.*, 2007]. It should be noted that the radiosonde data obtained from aboard the vessel were not sent through the Global Telecommunication System (GTS) of the World

Meteorological Organization (WMO), and thus are not included in these global analysis data. There is no substantial difference among the four analysis data sets at this level for this period. We find reasonable agreement between radiosonde observations and the analysis data for the whole period for meridional wind and in the second half of the period for temperature and zonal wind; however, between 22 November and 1 December, when the TTL was strongly affected by the passage of the Kelvin wave packet, there occur discrepancies in temperature and zonal wind. Although the phase of the wave packet is reasonably captured by all the analysis data, the amplitude is much smaller than that of the radiosonde observations. The analysis data do not represent the strong warm anomalies due to the downward stratospheric air transport by the wave packet. The difference in zonal wind is occasionally $>\sim 10$ m s^{-1}, which may be excessively large for certain purposes. For the other two campaigns, where the large-scale wave activity was weaker, the ECMWF operational analysis data generally agree with the radiosonde observations in the TTL.

4.3. December 2004 to January 2005 Campaign

4.3.1. Thick, Visual Cirrus

[30] Cirrus variations in the TTL during the first half of the December 2004 to January 2005 campaign can be interpreted in terms of the passage of a large-scale eastward moving wave, similar to that observed during the 2002 campaign. Figures 3 and 5 show that around 15–20 December, the TTL was influenced by a warm, downward displacement phase of the wave and was free of clouds. At around 21–31 December, when a cold phase of the wave was located over the vessel, cirrus clouds were observed in the TTL; however, the large-scale wave activity cannot explain the existence of thick cirrus clouds in the TTL during early January, when the TTL was again influenced by a warm phase of the wave.

[31] Figure 13 shows the frequency of deep convection reaching the 210 K temperature level (i.e., $\sim$13.5–14 km) or above, based on GOES 9 blackbody temperature (Tbb) data (at the infrared IR1 channel) and backward trajectories at 360 K for late December and early January. During these periods, an organized convective system with a zonal scale of $\sim$30° ($\sim$3,000 km) moved eastward along Java and the New Guinea islands to the southern tropical western Pacific at a speed of $\sim$40° per 8 days (i.e., $\sim$6 m s^{-1}). Thus, this convective system is regarded as the MJO. The vessel was located to the north of the main convective system. The thick, visual cirrus observed over the vessel in early January originated from the organized convection, particularly in the South Pacific Convergence Zone (SPCZ). The wet air injected into the TTL (and/or cirrus particles generated in the TTL) over the SPCZ were transported horizontally to the observation site within 1–2 days. In addition, the influence of midlatitude stratosphere, a drying factor for the TTL, was negligible for this campaign (see section 4.1 and Figures 9 and 10). Note that the subtropical portion of the trajectories in Figure 13 is considered less meaningful because the air mass identity is almost lost after encountering the region directly affected by deep convection.

[32] In summary, the tropical convective systems over the western Pacific generate Kelvin wave packets and horizontal outflows in the TTL [e.g., *Matsuno*, 1966; *Gill*, 1980]. The former directly control the generation and disappearance of cirrus in the TTL, whereas the latter, which can be regarded as part of the equatorial Rossby wave response to the organized convection, transport cirrus particles to off-equatorial regions.

4.3.2. Diurnal Variations

[33] During early January 2005, cirrus in the TTL showed regular diurnal variations with regular, apparent sedimentation during the nighttime. Figure 14 shows the time-altitude distributions of lidar cirrus signal β_{1064}, β_{1064}/β_{532}, the particle depolarization ratio at 532 nm, and the time series of optical depth at 1064 nm between 30 December 2004 and 9 January 2005. On almost every day during this period, cloud signals descended from the upper TTL in the evening to $\sim$10 km in the morning, with a descending speed of $\sim$10 km d^{-1} or $\sim 1 \times 10^{-1}$ m s^{-1}. The value of β_{1064}/β_{532} possibly shows a slight decrease with increasing altitude; the depolarization ratio shows a clear increase with increasing altitude. The optical depth may have ranged from $\sim 1 \times 10^{-2}$ (subvisual) to $\sim 5 \times 10^{-1}$ (visual). For the 2001 campaign, as stated above, *Iwasaki et al.* [2004] reported that observed subvisual cirrus showed apparent sedimentation at 2.6 km d^{-1} or 3×10^{-2} m s^{-1} on average during the nighttime. For the 2002 campaign, cirrus in the upper troposphere and in the TTL around 22–26 November, the first cold phase of equatorial Kelvin waves, also showed apparent sedimentation, although the descending rate and local time dependency were not as regular as the cases observed during the 2004–2005 campaign. Therefore, the nighttime apparent sedimentation is possibly one of the general characteristics of cirrus in the TTL. It should be noted that *Sassen et al.* [2008] presented midnight versus midday differences for global cirrus frequency using satellite-borne cloud radar and lidar and showed higher frequencies at midnight compared to midday in the tropics; the tendency is consistent with our observations in Figure 14 if we take the data around midnight and around midday only.

[34] Figure 15 shows the time-altitude distribution of normalized anomaly of WVMR and the average WVMR profile estimated from RS92 RH measurements (see section 2 for details of the estimation procedure). We observe a similar downward propagation of wet/dry anomaly signals, with wet regions and cloud regions generally overlapping in the TTL. Although the WVMR panels should basically be considered as a qualitative view, we observe ±(20–40)% variability at 14–16 km with average WVMR of $\sim$3 ppmv at 16 km, $\sim$10 ppmv at 15 km, and $\sim$20 ppmv at 14 km. Note that RH over ice in the wet anomaly regions in the TTL is often above 100% and sometimes $\sim$120%. This is due either to the uncertainty of measurements and estimation procedure or to the actual supersaturation recently often reported from measurements in the TTL [e.g., *Peter et al.*, 2006]. Figure 15 also shows the time-altitude distribution of temperature anomaly and the average temperature profile. The temperature data, in contrast, may indicate that the variability with a time scale of several days may generally be greater than the diurnal component in the TTL. In the following, we investigate two dynamical processes that may be relevant to the observed diurnal variations in cirrus within the TTL, namely, horizontal advection together with

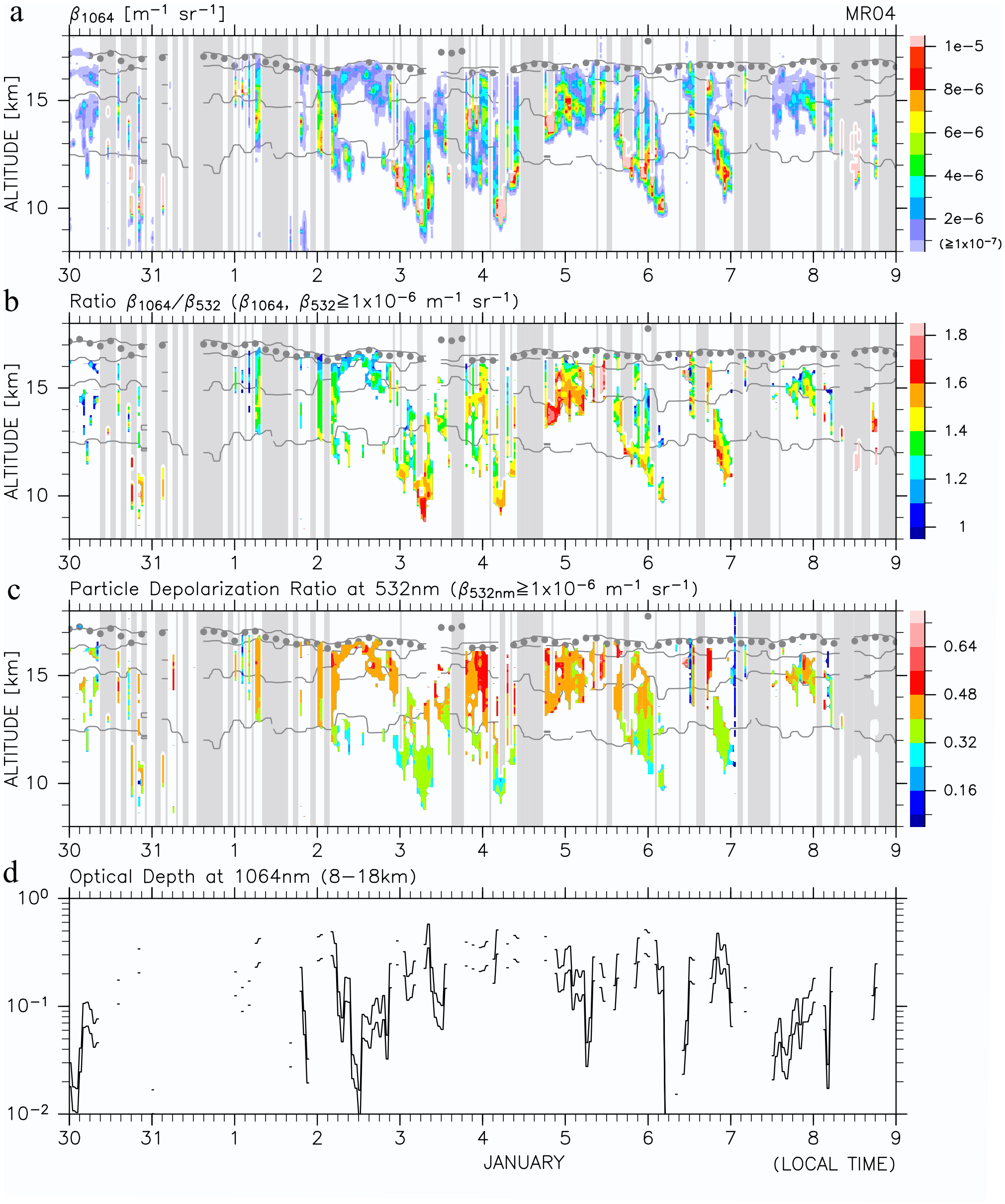

Figure 14. Time-altitude distributions of (a) β_{1064}, (b) β_{1064}/β_{532}, (c) the particle depolarization ratio at 532 nm, and (d) time series of estimated optical depth at 1064 nm for 8–18 km (with S = 15 sr and 25 sr) between 30 December 2004 (0000 LT) and 9 January 2005 (0000 LT). Note that the time shown here is local time (LT) at the observation site. For Figures 14a–14c, regions of missing measurements are colored light gray, the location of the cold-point tropopause is shown by gray dots, and the potential temperature levels of 370, 360, 355, and 350 K are indicated by gray lines.

diurnal variations in convective activity and diurnal variations in local temperature.

[35] Diurnal variations in deep convective activity within the SPCZ may lead to diurnal variations in cirrus within the remote TTL, as the SPCZ is the very source of water for the observed cirrus (Figure 13). Figure 16 shows the time series of high-cloud frequency for the SPCZ region between 29 December and 9 January. For the period after 31 December, when the eastward moving organized convection reached the SPCZ, we observe regular diurnal variations, with maximum activity before dawn (0300–0600 LT) and minimum activity in the late afternoon (1500–1800 LT). This early-morning maximum is one of the characteristics of deep convection in the tropical open oceans [e.g., *Imaoka and Spencer*, 2000, and references therein]. If horizontal winds in the TTL over the region including the SPCZ and the location of the vessel would have been steady with a slight positive vertical shear, the wet-dry contrast over the SPCZ region due to diurnal variations in wet air injection might have caused diurnally descending signals in cirrus over the vessel through the horizontal advection process. Figure 17 shows the time-altitude distributions of wind speed and direction measured with the radiosondes on the vessel. In the TTL, there is large variability in wind speed both in time and height; the speed varies with the period of 1–2 days with the maximum to

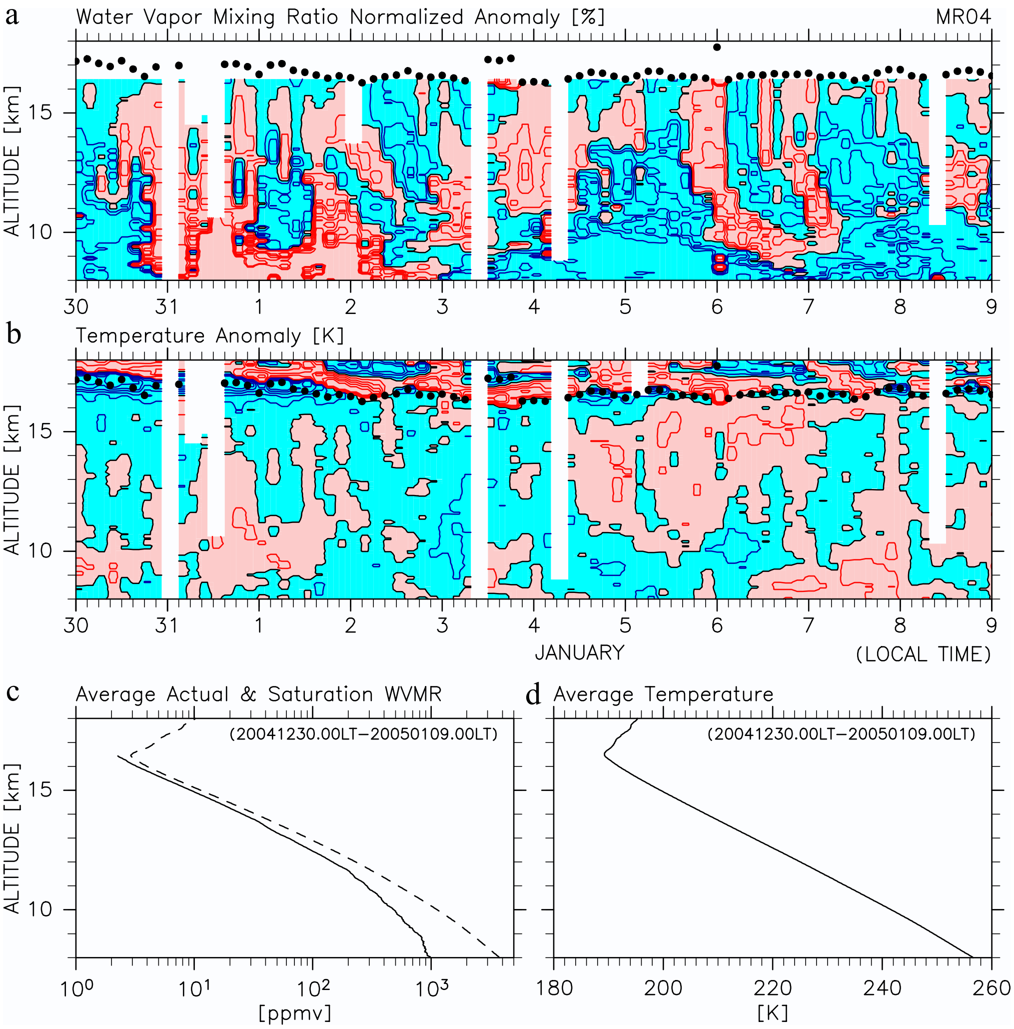

Figure 15. Time-altitude distributions of (a) water vapor mixing ratio (WVMR) anomaly normalized by the average and (b) temperature anomaly between 30 December 2004 (0000 LT) and 9 January 2005 (0000 LT) (times are local time). (c) The profiles of average WVMR (solid) and average ice saturation WVMR calculated from individual temperature and pressure profiles (dotted) and (d) the profile of average temperature. Averages are taken between 30 December 2004 (0000 LT) and 9 January 2005 (0000 LT). In Figures 15a and 15b, positive regions are colored light pink with red contours, negative regions are colored light blue with blue contours, and the location of the cold-point tropopause is shown by black dots. In Figure 15a, the contour interval is 25%, and contours between −125% and 125% are only shown (regions with <−125% or >125% may exist below 11 km). In Figure 15b, the contour interval is 1 K. See text for details of the calculation procedures of WVMR from RS92 radiosonde relative humidity data.

minimum difference of ~10 m s^{-1}, and the vertical shear is sometimes ~10 m s^{-1} per km. The wind direction is west–northwestward to northwestward, being consistent with the trajectories in Figure 13. If we take 2,000 km (~20°) for the distance between the northwestern edge of SPCZ and the vessel (Figure 13), a wind speed of 25 (15) m s^{-1} corresponds to a transport time of 22 (37) h. This means that the transport time (in hours) is likely to differ significantly for different trajectories starting on different day and at different height over the SPCZ. Therefore, the horizontal advection process alone is unlikely to explain the regular diurnal variations in cirrus, which are roughly fixed at specific local times, within the remote TTL. In the following, we hypothesize that the regular descending signals in cirrus are due to sedimentation that occurred simultaneously over a broad region including the northwestern edge of the SPCZ and the location of the vessel. Although Figure 15 shows that the amplitude of the diurnal component of temperature variations in the TTL may generally be smaller than that of longer time scale components, we investigate diurnal variations in local temperature that might have caused or at least supported the nighttime sedimentation.

[36] Figure 18 shows the local time composite of temperature anomaly between 30 December and 10 January, based on RS92 radiosonde data. The diurnal component is remarkable both in the troposphere and in the lower stratosphere, and its amplitude is greater than the overall uncertainty of the measurements (see section 2). Between

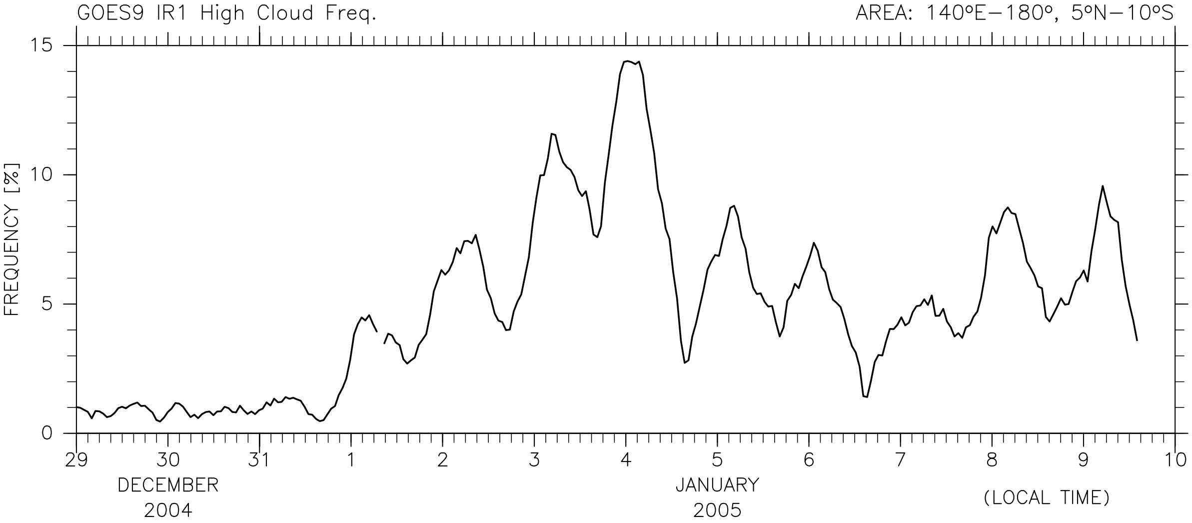

Figure 16. Time series of high-cloud frequency in percent (i.e., the frequency of blackbody temperatures <210 K at 0.25° × 0.25° grid points) for the SPCZ region (5°N–10°S, 140°E–180°) for 29 December 2004 to 9 January 2005 (times are local time) based on GOES 9 IR1 data.

~5.5 and ~15 km, the temperature shows a maximum from the daytime through early evening, and a minimum from midnight to early morning; the amplitude is 0.2–0.4 K. Above 18 km, the phase becomes earlier with altitude (e.g., at 20 km, the maximum is located around 0900–1200 LT), and the amplitude is ≥0.5 K. Around the tropopause, at 16.5–17.5 km, the amplitude is ~1 K, and the warmest (coldest) phase is around local midnight (noon). Around the tropopause for the period 14–29 December (not shown), in contrast, the amplitude is much smaller, being ~0.5 K, and the phase is strongly disturbed by higher-frequency components. The characteristics of observed diurnal variations in the middle to upper troposphere and in the lower stratosphere are consistent with the migrating diurnal tide

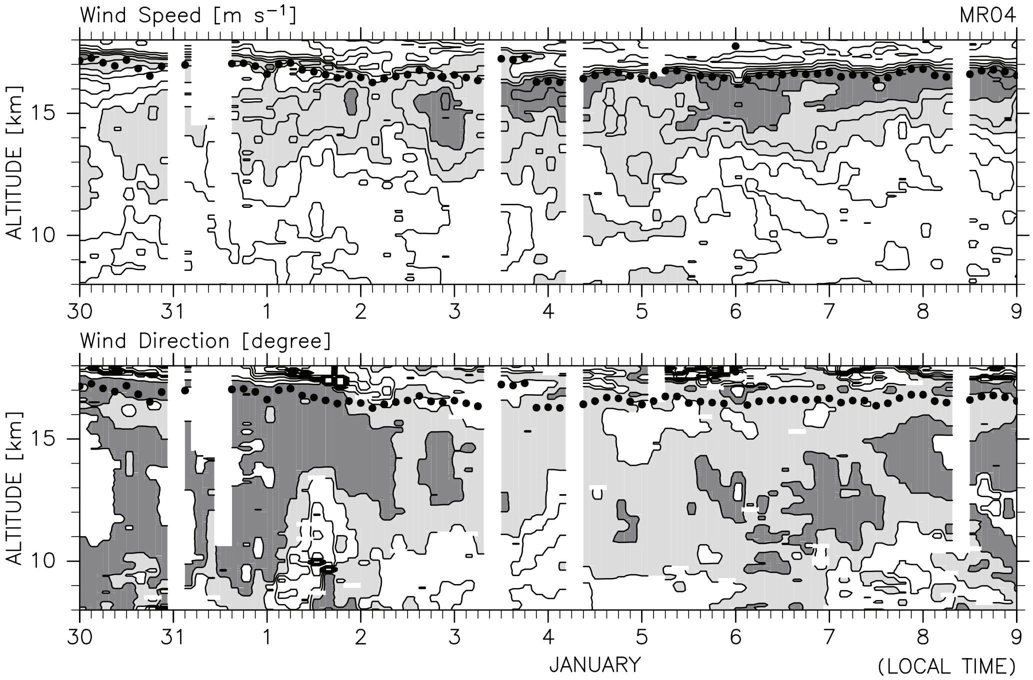

Figure 17. Time-altitude distributions of (top) horizontal wind speed and (bottom) direction between 30 December 2004 (0000 LT) and 9 January 2005 (0000 LT) (times are local time). In Figure 17 (top), the contour interval is 5 m s^{-1}, the regions with 15–25 m s^{-1} are colored light gray, and those with >25 m s^{-1} are colored dark gray. In Figure 17 (bottom), the contour interval is 30°, the regions with 90°–120° are colored light gray, and those with 120°–150° are colored dark gray. The wind direction is defined as 0° for southward and 90° for westward. In both panels, the location of the cold-point tropopause is shown by black dots.

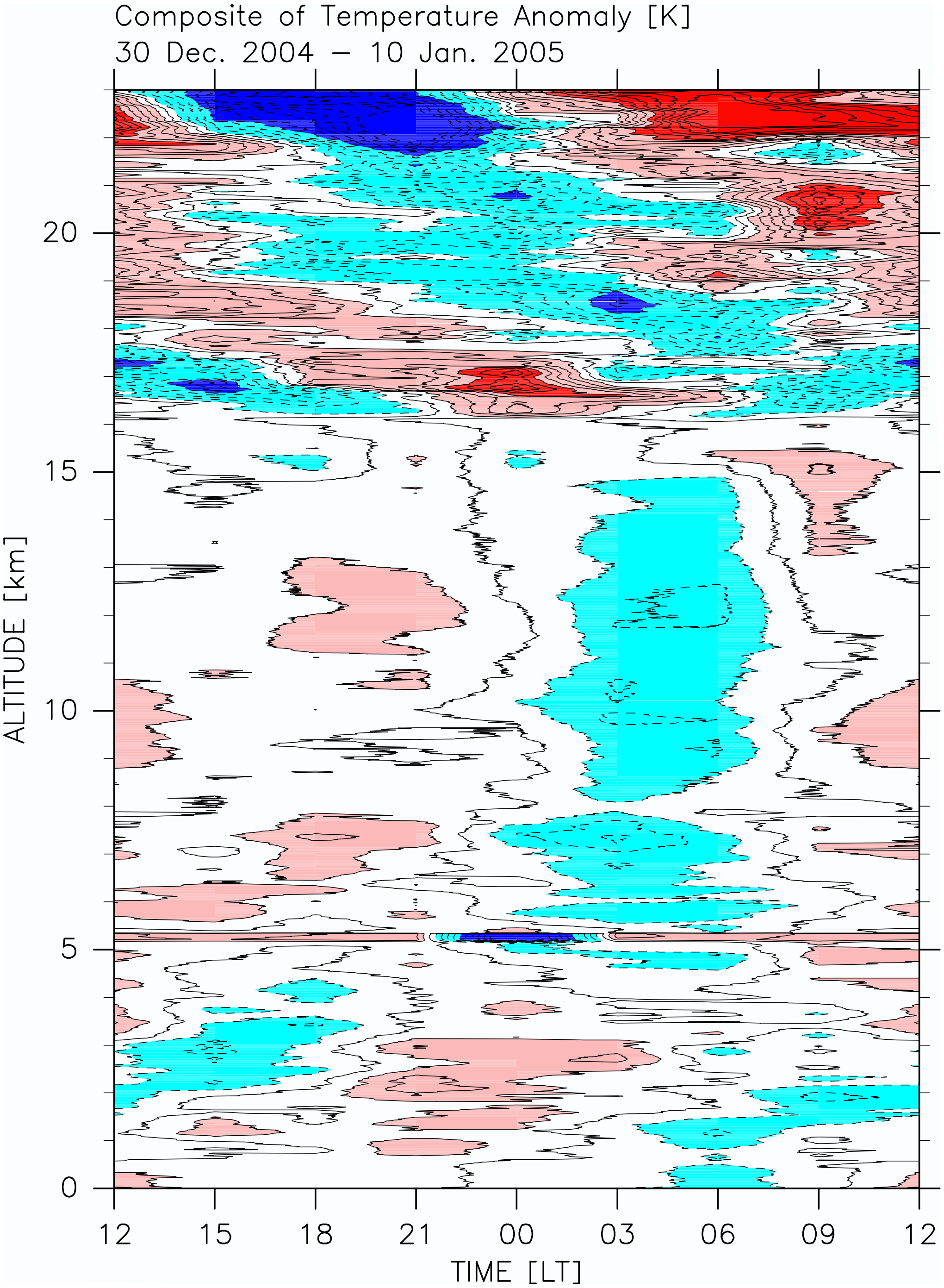

Figure 18. Composite of temperature anomaly onto the local time between 30 December 2004 and 10 January 2005 based on radiosonde data. The averages are taken for the same period. The contour interval is 0.2 K, and negative contours are dashed. The regions with >1 K (<−1 K) are colored red (blue), and those with 0.2–1 K (−0.2 to −1 K) are colored light red (light blue).

(i.e., the westward moving, zonal wave number one diurnal tide) revealed by Global Positioning System (GPS) temperature data and model simulations [*Zeng et al.*, 2008], by tropical radiosonde measurements [*Alexander and Tsuda*, 2008], and by four-times-daily JRA25/JCDAS reanalysis temperature data (not shown). The significant diurnal variations observed around the tropopause between 30 December and 10 January may have arisen from a combination of the migrating tide and the regional-scale convective activity discussed previously; diurnal variations in deep convection within the SPCZ may have generated gravity waves with a period of 24 h similar to the ones studied by *Kawatani et al.* [2003].

[37] The potential contribution of the temperature variations shown in Figure 18 to cirrus variations is as follows. The daytime temperature minimum near the tropopause provides a favorable condition for cirrus formation; however, the warmer conditions in the lower TTL may tend to

evaporate cirrus particles. The midnight temperature maximum near the tropopause tends to prevent cirrus formation, but the colder conditions in the lower TTL allow falling cirrus particles to be maintained or even grow. These statements provide a qualitative explanation of all the major characteristics of the observed diurnal variations in cirrus within the TTL. It should be noted, however, that ±(0.2–0.4) K (±1 K) temperature changes result in ±5% (±20%) saturation WVMR changes in the TTL, and cannot fully explain the ±(20–40)% WVMR variability estimated from RS92 RH data.

[38] A full explanation of the observed diurnal variations in cirrus requires a consideration of cloud microphysics and solar and infrared radiative processes, as well as dynamical processes. *Jensen et al.* [1996] performed numerical simulations of cirrus clouds initially located near the tropical tropopause, incorporating detailed microphysical and radiative processes. The results of one of their simulations, considering the outflow from cumulonimbus cirrus anvils with an initial optical thickness of ~10 and a high initial ice water content (IWC) (0.05 g m^{-3} at 15.6–17 km), are similar to our observations. In this simulation case, the largest particles, with a radius of 30–50 μm, descended to 13–14 km in ~4 h. Other simulations, with a lower initial IWC or a smaller initial optical thickness, for example, show a smaller vertical extent of sedimentation over 24 h. When the authors assigned a background uplift of 1×10^{-2} m s^{-1} due to, for example, upward winds induced by equatorial Kelvin waves, the cirrus clouds tended to persist near the tropopause. If these simulations were to take into account diurnal variations in temperature due to the dynamical processes discussed above, the results may be in better agreement with our observations.

5. Conclusions

[39] We conducted cirrus measurements in the TTL over the tropical western Pacific during three northern winters using a shipborne lidar system, and observed various behaviors of cirrus with time scales ranging from several hours to several days. Using various meteorological data sets, we discussed the controlling processes for the observed cirrus variations, mainly from the viewpoint of large-scale meteorology. During the 2001 campaign, the TTL was constantly cold over the vessel, but was often cloud-free, with only some subvisual cirrus clouds. Trajectory and PV analyses revealed that the TTL during this campaign was strongly affected by dry air transport from the northern midlatitude lower stratosphere. This factor, together with low wave activity in the local TTL, is probably the main reason for the observed quasi-cloud-free TTL. During the 2002 campaign, a packet of large-amplitude Kelvin waves was found to control both the generation and disappearance of cirrus in the TTL. During the 2004–2005 campaign, thick, visual cirrus clouds were observed in the TTL. A cold phase of large-scale eastward moving waves contributed to cirrus generation and maintenance during the middle of the campaign period, and the horizontal transport of wet air injected over the SPCZ 1–2 days beforehand resulted in cirrus formation later in the campaign period. In early January 2005, we observed regular diurnal variations in cirrus within the TTL; namely, apparent sedimentation during the nighttime at a speed of $\sim 1 \times 10^{-1}$ m s^{-1}. We discussed two possible controlling processes, namely, horizontal advection together with diurnal variations in convective activity within the source region and diurnal variations in local temperature due to tides and gravity waves.

[40] The source of cirrus in the TTL is water vapor and cloud particles in the lower to middle troposphere, primarily transported vertically by deep convection with a time scale of ~1 h. Rapid horizontal transport in the TTL, with a typical speed of 10 m s^{-1}, can connect the convective-free region to the source region at a distance of 1,000–10,000 km, as far as the identity of the air mass is retained. When the TTL is influenced by large-amplitude equatorial Kelvin waves, as is often the case, particularly in the Indian Ocean through the Indonesian maritime continent to the Pacific, cirrus generation and disappearance are strongly controlled by the phase of these waves. At the cold and upward displacement phase of the waves, cirrus clouds are present, and are possibly involved in the interaction among dynamics, cloud microphysics, and radiation. At the warm and downward displacement phase, in contrast, cirrus clouds disappear, and the TTL is dominated by dry stratospheric air. When the TTL is influenced by quasi-horizontal dry air transport from the midlatitudes via Rossby wave breaking events, the TTL tends to be cloud-free. A full interpretation of the cirrus observations in the TTL requires consideration of these four processes, namely, (1) convective transport of water (vapor and ice), (2) horizontal transport of water (associated with, for example, equatorial Rossby waves generated by organized convection), (3) large-amplitude equatorial Kelvin waves generated by organized convection, and (4) dry air transport from the midlatitude lower stratosphere. Process 4 was important during the 2001 campaign, process 3 was important during the 2002 campaign, and processes 3 (for late December) and 1 and 2 (for early January) were important during the 2004–2005 campaign.

[41] Finally, by making continuous, 1-month lidar measurements during three northern winters, we have revealed the characteristics of diurnal variations in cirrus within the TTL. Nighttime apparent sedimentation at a speed of 10^{-2}–10^{-1} m s^{-1} may be a general characteristic of cirrus in the TTL, regardless of optical depth. This daily, regular process is possibly one of the important dehydration processes for the stratosphere. Although the nature of the mechanism remains an open question, we have identified some relevant phenomena for the prominent cases observed during the second half of the 2004–2005 campaign. Radiosonde water vapor data indicate that wet signals are generally in phase with the descending cloud signals. Deep convective activity in the SPCZ, the source region of the observed cirrus, showed regular diurnal variations, with the maximum before dawn. If conditions in horizontal winds within the TTL were favorable, the diurnal wet-dry contrast created over the SPCZ might have resulted in apparent sedimentation over the vessel through the horizontal advection process. However, estimation of transport time using radiosonde wind data revealed that this process alone cannot explain the observed phase of cirrus variation. Radiosonde temperature data also showed significant diurnal variations in the troposphere through the lower stratosphere, particularly during the period when regular cirrus variations were

observed. The temperature variations probably arose from the migrating diurnal tide, with an additional contribution from gravity waves generated by regular convection in the SPCZ. The phase profile of temperature in the TTL provides a qualitative explanation of the observed diurnal variations in cirrus. Numerical experiments that consider the interaction among microphysics, radiation, and the dynamical processes discussed in this paper would provide further insights into cirrus behavior in the TTL.

[42] **Acknowledgments.** The authors thank the technical staff of Global Ocean Development Inc. for their support with observations from on board the Mirai. The interpolated OLR data and the NCEP1 and NCEP2 reanalysis data were provided by the NOAA/OAR/ESRL PSD. The JRA25/JCDAS data were provided by the JMA and CRIEPI. The GOES 9 data were obtained from Kochi University. Figures 1–18 were produced using the GFD-DENNOU Library. We thank two anonymous referees for constructive reviews. This study was supported in part by the Japan Agency for Marine-Earth Science and Technology; the Japanese Ministry of Education, Culture, Sports, Science and Technology (MEXT) through Grants-in-Aid for Scientific Research (15204043, 16740264, 18204041, and 19740283); the Ministry of the Environment through the Global Environment Research Fund (A-1 and A-071); the Japan Science and Technology Agency (JST) through the Core Research for Evolutional Science and Technology; and the Inoue Foundation for Science.

References

Ackerman, T. P., K.-N. Liou, F. P. J. Valero, and L. Pfister (1988), Heating rates in tropical anvils, *J. Atmos. Sci.*, *45*(10), 1606–1623.

Alexander, S. P., and T. Tsuda (2008), Observations of the diurnal tide during seven intensive radiosonde campaigns in Australia and Indonesia, *J. Geophys. Res.*, *113*, D04109, doi:10.1029/2007JD008717.

Andrews, D. G., J. R. Holton, and C. B. Leovy (1987), *Middle Atmosphere Dynamics*, 489 pp., Academic, San Diego, Calif.

Boehm, M. T., and J. Verlinde (2000), Stratospheric influence on upper tropospheric tropical cirrus, *Geophys. Res. Lett.*, *27*(19), 3209–3212, doi:10.1029/2000GL011678.

Comstock, J. M., T. P. Ackerman, and G. G. Mace (2002), Ground-based lidar and radar remote sensing of tropical cirrus clouds at Nauru Island: Cloud statistics and radiative impacts, *J. Geophys. Res.*, *107*(D23), 4714, doi:10.1029/2002JD002203.

Corti, T., B. P. Luo, Q. Fu, H. Vömel, and T. Peter (2006), The impact of cirrus clouds on tropical troposphere-to-stratosphere transport, *Atmos. Chem. Phys.*, *6*, 2539–2547.

Danielsen, E. F. (1982), A dehydration mechanism for the stratosphere, *Geophys. Res. Lett.*, *9*(6), 605–608.

Danielsen, E. F. (1993), In situ evidence of rapid, vertical, irreversible transport of lower tropospheric air into the lower tropical stratosphere by convective cloud turrets and by larger-scale upwelling in tropical cyclones, *J. Geophys. Res.*, *98*(D5), 8665–8681.

Dessler, A. E., S. P. Palm, W. D. Hart, and J. D. Spinhirne (2006a), Tropopause-level thin cirrus coverage revealed by ICESat/Geoscience Laser Altimeter System, *J. Geophys. Res.*, *111*, D08203, doi:10.1029/2005JD006586.

Dessler, A. E., S. P. Palm, and J. D. Spinhirne (2006b), Tropical cloud-top height distributions revealed by the Ice, Cloud, and Land Elevation Satellite (ICESat)/Geoscience Laser Altimeter System (GLAS), *J. Geophys. Res.*, *111*, D12215, doi:10.1029/2005JD006705.

Doherty, G. M., R. E. Newell, and E. F. Danielsen (1984), Radiative heating rates near the stratospheric fountain, *J. Geophys. Res.*, *89*(D1), 1380–1384.

Eguchi, N., and K. Kodera (2007), Impact of the 2002, Southern Hemisphere, stratospheric warming on the tropical cirrus clouds and convective activity, *Geophys. Res. Lett.*, *34*, L05819, doi:10.1029/2006GL028744.

Eguchi, N., and M. Shiotani (2004), Intraseasonal variations of water vapor and cirrus clouds in the tropical upper troposphere, *J. Geophys. Res.*, *109*, D12106, doi:10.1029/2003JD004314.

Eguchi, N., T. Yokota, and G. Inoue (2007), Characteristics of cirrus clouds from ICESat/GLAS observations, *Geophys. Res. Lett.*, *34*, L09810, doi:10.1029/2007GL029529.

Fu, Q., Y. Hu, and Q. Yang (2007), Identifying the top of the tropical tropopause layer from vertical mass flux analysis and CALIPSO lidar cloud observations, *Geophys. Res. Lett.*, *34*, L14813, doi:10.1029/2007GL030099.

Fujiwara, M., and M. Takahashi (2001), Role of the equatorial Kelvin wave in stratosphere-troposphere exchange in a general circulation model, *J. Geophys. Res.*, *106*(D19), 22,763–22,780.

Fujiwara, M., K. Kita, and T. Ogawa (1998), Stratosphere-troposphere exchange of ozone associated with the equatorial Kelvin wave as observed with ozonesondes and rawinsondes, *J. Geophys. Res.*, *103*(D15), 19,173–19,182.

Fujiwara, M., F. Hasebe, M. Shiotani, N. Nishi, H. Vömel, and S. J. Oltmans (2001), Water vapor control at the tropopause by equatorial Kelvin waves observed over the Galápagos, *Geophys. Res. Lett.*, *28*(16), 3143–3146.

Fujiwara, M., M. Shiotani, F. Hasebe, H. Vömel, S. J. Oltmans, P. W. Ruppert, T. Horinouchi, and T. Tsuda (2003a), Performance of the Meteolabor "Snow White" chilled-mirror hygrometer in the tropical troposphere: Comparisons with the Vaisala RS80 A/H-Humicap sensors, *J. Atmos. Oceanic Technol.*, *20*, 1534–1542.

Fujiwara, M., et al. (2003b), Ozonesonde observations in the Indonesian maritime continent: A case study on ozone rich layer in the equatorial upper troposphere, *Atmos. Environ.*, *37*(3), 353–362.

Fujiwara, M., M. K. Yamamoto, H. Hashiguchi, T. Horinouchi, and S. Fukao (2003c), Turbulence at the tropopause due to breaking Kelvin waves observed by the Equatorial Atmosphere Radar, *Geophys. Res. Lett.*, *30*(4), 1171, doi:10.1029/2002GL016278.

Gettelman, A., and P. M. de F. Forster (2002), A climatology of the tropical tropopause layer, *J. Meteorol. Soc. Jpn.*, *80*(4B), 911–924.

Gill, A. E. (1980), Some simple solutions for heat-induced tropical circulation, *Q. J. R. Meteorol. Soc.*, *106*, 447–462.

Hartmann, D. L., J. R. Holton, and Q. Fu (2001), The heat balance of the tropical tropopause, cirrus and stratospheric dehydration, *Geophys. Res. Lett.*, *28*(10), 1969–1972.

Hasebe, F., M. Fujiwara, N. Nishi, M. Shiotani, H. Vömel, S. Oltmans, H. Takashima, S. Saraspriya, N. Komala, and Y. Inai (2007), In situ observations of dehydrated air parcels advected horizontally in the tropical tropopause layer of the western Pacific, *Atmos. Chem. Phys.*, *7*, 803–813.

Hatsushika, H., and K. Yamazaki (2003), Stratospheric drain over Indonesia and dehydration within the tropical tropopause layer diagnosed by air parcel trajectories, *J. Geophys. Res.*, *108*(D19), 4610, doi:10.1029/2002JD002986.

Highwood, E. J., and B. J. Hoskins (1998), The tropical tropopause, *Q. J. R. Meteorol. Soc.*, *124*, 1579–1604.

Holton, J. R. (1984), Troposphere-stratosphere exchange of trace constituents: The water vapor puzzle, in *Dynamics of the Middle Atmosphere*, edited by J. R. Holton and T. Matsuno, pp. 369–385, Terra Sci., Tokyo.

Holton, J. R., and A. Gettelman (2001), Horizontal transport and the dehydration of the stratosphere, *Geophys. Res. Lett.*, *28*(14), 2799–2802, doi:10.1029/2001GL013148.

Imaoka, K., and R. W. Spencer (2000), Diurnal variation of precipitation over the tropical oceans observed by TRMM/TMI combined with SSM/I, *J. Clim.*, *13*, 4149–4158.

Immler, F., K. Krüger, S. Tegtmeier, M. Fujiwara, P. Fortuin, G. Verver, and O. Schrems (2007), Cirrus clouds, humidity, and dehydration in the tropical tropopause layer observed at Paramaribo, Suriname (5.8°N, 55.2°W), *J. Geophys. Res.*, *112*, D03209, doi:10.1029/2006JD007440.

Immler, F., K. Krüger, M. Fujiwara, G. Verver, M. Rex, and O. Schrems (2008), Correlation between equatorial Kelvin waves and the occurrence of extremely thin ice clouds at the tropical tropopause, *Atmos. Chem. Phys.*, *8*, 4019–4026.

Iwasaki, S., et al. (2004), Subvisual cirrus cloud observations using a 1064-nm lidar, a 95 GHz cloud radar, and radiosondes in the warm pool region, *Geophys. Res. Lett.*, *31*, L09103, doi:10.1029/2003GL019377.

Jensen, E., and L. Pfister (2004), Transport and freeze-drying in the tropical tropopause layer, *J. Geophys. Res.*, *109*, D02207, doi:10.1029/2003JD004022.

Jensen, E. J., O. B. Toon, H. B. Selkirk, J. D. Spinhirne, and M. R. Schoeberl (1996), On the formation and persistence of subvisible cirrus clouds near the tropical tropopause, *J. Geophys. Res.*, *101*(D16), 21,361–21,375.

Johnston, H. S., and S. Solomon (1979), Thunderstorms as possible micrometeorological sink for stratospheric water, *J. Geophys. Res.*, *84*(C6), 3155–3158.

Kanamitsu, M., W. Ebisuzaki, J. Woollen, S.-K. Yang, J. J. Hnilo, M. Fiorino, and G. L. Potter (2002), NCEP-DEO AMIP-II reanalysis (R-2), *Bull. Am. Meteorol. Soc.*, *83*(11), 1631–1643.

Kalnay, E., et al. (1996), The NCEP/NCAR 40-year reanalysis project, *Bull. Am. Meteorol. Soc.*, *77*(3), 437–471.

Kawatani, Y., S. K. Dhaka, M. Takahashi, and T. Tsuda (2003), Large potential energy of gravity waves over a smooth surface with little convection: Simulation and observation, *Geophys. Res. Lett.*, *30*(8), 1438, doi:10.1029/2003GL016960.

Liebmann, B., and C. A. Smith (1996), Description of a complete (interpolated) outgoing longwave radiation dataset, *Bull. Am. Meteorol. Soc.*, *77*(6), 1275–1277.

Luers, J. K. (1997), Temperature error of the Vaisala RS90 radiosonde, *J. Atmos. Oceanic Technol.*, *14*, 1520–1532.

Luo, B. P., et al. (2003), Dehydration potential of ultrathin clouds at the tropical tropopause, *Geophys. Res. Lett.*, *30*(11), 1557, doi:10.1029/2002GL016737.

Lynch, D. K., and K. Sassen (2002), Subvisual cirrus, in *Cirrus*, edited by D. K. Lynch et al., pp. 256–264, Oxford Univ. Press, New York.

Mace, G. G., M. Deng, B. Soden, and E. Zipser (2006), Association of tropical cirrus in the 10–15-km layer with deep convective sources: An observational study combining millimeter radar data and satellite-derived trajectories, *J. Atmos. Sci.*, *63*, 480–503.

Madden, R. A., and P. R. Julian (1994), Observations of the 40–50-day tropical oscillation-A review, *Mon. Weather Rev.*, *122*, 814–837.

Massie, S., A. Gettelman, W. Randel, and D. Baumgardner (2002), Distribution of tropical cirrus in relation to convection, *J. Geophys. Res.*, *107*(D21), 4591, doi:10.1029/2001JD001293.

Matsuno, T. (1966), Quasi-geostrophic motions in the equatorial area, *J. Meteorol. Soc. Jpn.*, *44*(1), 25–43.

McFarquhar, G. M., A. J. Heymsfield, J. Spinhirne, and B. Hart (2000), Thin and subvisual tropopause tropical cirrus: Observations and radiative impacts, *J. Atmos. Sci.*, *57*(12), 1841–1853.

Miloshevich, L. M., A. Paukkunen, H. Vömel, and S. J. Oltmans (2004), Development and validation of a time-lag correction for Vaisala radiosonde humidity measurements, *J. Atmos. Oceanic Technol.*, *21*(12), 1305–1327.

Murphy, D. M., and T. Koop (2005), Review of the vapour pressures of ice and supercooled water for atmospheric applications, *Q. J. R. Meteorol. Soc.*, *131*, 1539–1565.

Newman, P. A., and M. R. Schoeberl (1995), A reinterpretation of the data from the NASA stratosphere-troposphere exchange project, *Geophys. Res. Lett.*, *22*(18), 2502–2504.

Nishi, N., J. Suzuki, A. Hamada, and M. Shiotani (2007), Rapid transitions in zonal wind around the tropical tropopause and their relation to the amplified equatorial Kelvin waves, *Sci. Online Lett. Atmos.*, *3*, 13–16.

Okamoto, H., et al. (2007), Vertical cloud structure observed from shipborne radar and lidar: Midlatitude case study during the MR01/K02 cruise of the research vessel Mirai, *J. Geophys. Res.*, *112*, D08216, doi:10.1029/2006JD007628.

Onogi, K., et al. (2007), The JRA-25 reanalysis, *J. Meteorol. Soc. Jpn.*, *85*(3), 369–432.

Parker, D. E. (1973), Equatorial Kelvin waves at 100 millibars, *Q. J. R. Meteorol. Soc.*, *99*(419), 116–129.

Peter, T., C. Marcolli, P. Spichtinger, T. Corti, M. B. Baker, and T. Koop (2006), When dry air is too humid, *Science*, *314*, 1399–1402, doi:10.1126/science.1135199.

Pfister, L., et al. (2001), Aircraft observations of thin cirrus clouds near the tropical tropopause, *J. Geophys. Res.*, *106*(D9), 9765–9786.

Platt, C. M. R., J. C. Scott, and A. C. Dilley (1987), Remote sounding of high clouds. Part VI: Optical properties of midlatitude and tropical cirrus, *J. Atmos. Sci.*, *44*(4), 729–747.

Postel, G. A., and M. H. Hitchman (1999), A climatology of Rossby wave breaking along the subtropical tropopause, *J. Atmos. Sci.*, *56*(3), 359–373.

Potter, B. E., and J. R. Holton (1995), The role of monsoon convection in the dehydration of the lower tropical stratosphere, *J. Atmos. Sci.*, *52*(8), 1034–1050.

Randel, W. J., F. Wu, A. Gettelman, J. M. Russell III, J. M. Zawodny, and S. J. Oltmans (2001), Seasonal variation of water vapor in the lower stratosphere observed in Halogen Occultation Experiment data, *J. Geophys. Res.*, *106*(D13), 14,313–14,325.

Robinson, G. D. (1980), The transport of minor atmospheric constituents between troposphere and stratosphere, *Q. J. R. Meteorol. Soc.*, *106*(448), 227–253.

Sassen, K., Z. Wang, and D. Liu (2008), Global distribution of cirrus clouds from CloudSat/Cloud-Aerosol Lidar and Infrared Pathfinder Satellite Observations (CALIPSO) measurements, *J. Geophys. Res.*, *113*, D00A12, doi:10.1029/2008JD009972.

Steinbrecht, W., H. Claude, F. Schönenborn, U. Leiterer, H. Dier, and E. Lanzinger (2008), Pressure and temperature differences between Vaisala RS80 and RS92 radiosonde systems, *J. Atmos. Oceanic Technol.*, *25*, 909–927.

Sugimoto, N., I. Matsui, A. Shimizu, I. Uno, K. Asai, T. Endoh, and T. Nakajima (2002), Observation of dust and anthropogenic aerosol plumes in the Northwest Pacific with a two-wavelength polarization lidar on board the research vessel Mirai, *Geophys. Res. Lett.*, *29*(19), 1901, doi:10.1029/2002GL015112.

Suzuki, J., and M. Shiotani (2008), Space-time variability of equatorial Kelvin waves and intraseasonal oscillations around the tropical tropopause, *J. Geophys. Res.*, *113*, D16110, doi:10.1029/2007JD009456.

Tsuda, T., Y. Murayama, H. Wiryosumarto, S. Harijono, and S. Kato (1994), Radiosonde observations of equatorial atmosphere dynamics over Indonesia: 1. Equatorial waves and diurnal tides, *J. Geophys. Res.*, *99*(D5), 10,491–10,505.

Verver, G., M. Fujiwara, P. Dolmans, C. Becker, P. Fortuin, and L. Miloshevich (2006), Performance of the Vaisala RS80 A/H and RS90 Humicap sensors and the Meteolabor Snow White chilled-mirror hygrometer in Paramaribo, Suriname, *J. Atmos. Oceanic Technol.*, *23*(11), 1506–1518.

Vömel, H., M. Fujiwara, M. Shiotani, F. Hasebe, S. J. Oltmans, and J. E. Barnes (2003), The behavior of the Snow White chilled-mirror hygrometer in extremely dry conditions, *J. Atmos. Oceanic Technol.*, *20*(11), 1560–1567.

Wang, P.-H., P. Minnis, M. P. McCormick, G. S. Kent, and K. M. Skeens (1996), A 6-year climatology of cloud occurrence frequency from Stratospheric Aerosol and Gas Experiment II observations (1985–1990), *J. Geophys. Res.*, *101*(D23), 29,407–29,430.

Waugh, D. W., and L. M. Polvani (2000), Climatology of intrusions into the tropical upper troposphere, *Geophys. Res. Lett.*, *27*(23), 3857–3860.

Wheeler, M., G. N. Kiladis, and P. J. Webster (2000), Large-scale dynamical fields associated with convectively coupled equatorial waves, *J. Atmos. Sci.*, *57*(5), 613–640.

Winker, D. M., and C. R. Trepte (1998), Laminar cirrus observed near the tropical tropopause by LITE, *Geophys. Res. Lett.*, *25*(17), 3351–3354.

Yoneyama, K., M. Fujita, N. Sato, M. Fujiwara, Y. Inai, and F. Hasebe (2008), Correction for radiation dry bias found in RS92 radiosonde data during the MISMO field experiment, *Sci. Online Lett. Atmos.*, *4*, 13–16.

Zeng, Z., W. Randel, S. Sokolovskiy, C. Deser, Y.-H. Kuo, M. Hagan, J. Du, and W. Ward (2008), Detection of migrating diurnal tide in the tropical upper troposphere and lower stratosphere using the Challenging Minisatellite Payload radio occultation data, *J. Geophys. Res.*, *113*, D03102, doi:10.1029/2007JD008725.

Zhang, C. (2005), Madden-Julian Oscillation, *Rev. Geophys.*, *43*, RG2003, doi:10.1029/2004RG000158.

M. Fujiwara, F. Hasebe, Y. Inai, and T. Sakazaki, Graduate School of Environmental Science, Hokkaido University, N10 W5, Sapporo 060-0810, Japan. (fuji@ees.hokudai.ac.jp)

A. Hamada and N. Nishi, Graduate School of Science, Kyoto University, Kyoto 606-8502, Japan.

S. Iwasaki, National Defense Academy, Hashirimizu 1-10-20, Yokosuka 239-8686, Japan.

I. Matsui, A. Shimizu, and N. Sugimoto, National Institute for Environmental Studies, Onogawa 16-2, Tsukuba 305-8506, Japan.

H. Okamoto, Graduate School of Science, Tohoku University, Aoba 6-3, Sendai 980-8578, Japan.

M. Shiotani, Research Institute for Sustainable Humanosphere, Kyoto University, Gokasho, Uji 611-0011, Japan.

K. Yoneyama, Japan Agency for Marine-Earth Science and Technology, Natsushima 2-15, Yokosuka 237-0061, Japan.